GaN-Based Megahertz Single-Phase Inverter With a Hybrid TCM Control Method for High Efficiency and High-Power Density

Teng Liu, *Student Member, IEEE*, Cai Chen, *Member, IEEE*, Ke Xu, Yi Zhang, and Yong Kang, *Senior Member, IEEE*

***Abstract*—Compared with traditional frequency limitation method DCM and QCFTCM for TCM-based inverter, this article proposes a hybrid TCM method, which can achieve both full range ZVS and frequency variation limitation. An accurate resonant transition model is established and the switching frequency variation range can be obtained for TCM. The hybrid control can be implemented according to the variation ratio γ. In order to determine the optimal γ, an offline optimization algorithm based on loss estimation is proposed. Therefore, an accurate analytical loss model for GaN HEMTs considering the nonlinear junction capacitance is given for TCM and hybrid TCM. The loss model shows that the total losses of hybrid TCM inverter are reduced compared with TCM. Moreover, an interleaved GaN-based megahertz single-phase inverter with digital control is demonstrated with 120 W/in^3 power density. The aforementioned benefits are experimentally verified in the optimal hybrid TCM. With this hybrid control, the measured peak efficiency is 98%. Compared with pure TCM mode, there is a 70% reduction in the switching frequency and the related efficiency is 0.8% higher at light loads. Higher power density (135 W/in^3) can be achieved in hybrid TCM through further increasing the switching frequency compared with pure TCM.**

***Index Terms*—Analytical model, high power density, Gallium nitride (GaN), triangular current modulation (TCM), single-phase H-bridge inverter, hybrid control method.**

I. Introduction

SINGLE-PHASE inverters are widely used in low power level (1–10 kW) industrial or residential applications, including photovoltaic (PV) inverters [1], fuel cell systems [2], and other power supplies [3]. For the commercial PV inverters from a broad range of above applications, the efficiency is usually as high as 96%–99% but the power density is usually between 2–15 W/in^3 [4]–[7]. The power density is mainly limited by low switching frequency due to the use of Silicon (Si) devices.

Manuscript received April 9, 2020; revised September 10, 2020; accepted November 10, 2020. Date of publication November 19, 2020; date of current version February 5, 2021. This work was supported in part by the National Natural Science Foundation of China under Grant 52077094. Recommended for publication by Associate Editor A. Safaee. *(Corresponding author: Cai Chen.)*

The authors are with the The State Key Laboratory of Advanced Electromagnetic Engineering and Technology, School of Electrical and Electronic Engineering, Huazhong University of Science and Technology, Wuhan 430074, China (e-mail: teng_liu@hust.edu.cn; caichen@hust.edu.cn; xu_ke@hust.edu.cn; d201880465@hust.edu.cn; ykang@hust.edu.cn).

Color versions of one or more of the figures in this article are available at https://doi.org/10.1109/TPEL.2020.3039386.

Digital Object Identifier 10.1109/TPEL.2020.3039386

For pushing higher switching frequency to achieve high power density, it is urgent to apply better power devices to replace Si devices. Recent emerging wide-band-gap power devices, such as gallium nitride (GaN) HEMTs, are expected to be promising candidates for high-frequency power conversion techniques. Due to the advantages of the material, the GaN HEMTs have the features of wide band gap, high electron mobility, and high electron velocity [8], [9]. Thus, better figure of merits can be projected for GaN HEMTs than for the state-of-the-art Si transistors, which allows GaN HEMTs to switch with faster transition speed and lower switching loss. Moreover, the zero reverse-recovery charge of enhancement-mode (e-mode) GaN HEMTs will decrease the related switching loss further. Therefore, instead of the traditional Si devices, the use of GaN HEMTs enable the converter to operate at high frequency, which will allow a reduction in the size and the volume of the system and relatively increase the inverter's power density [10].

Some hard-switching GaN-based inverters have been demonstrated in [11]–[14]. However, good efficiency only remains at 50–250 kHz in those hard-switching inverters, which is slightly better than Si-based inverters. For pushing higher switching frequency (up to megahertz) and achieving excellent system-level benefits, soft switching is required in GaN-based converters. Triangular current modulation (TCM) is one of the simple ways to achieve soft switching, which is first proposed in [15]. Combining with TCM, GaN-based converters can easily achieve ultrahigh efficiency at megahertz switching frequency. In the literature [16], a 1.2-kW megahertz dual-phase interleaved totem-pole PFC with TCM was demonstrated with 99% peak efficiency and 220 W/in^3 power density. The work in [17] also proposed a TCM-based bidirectional ac/dc converter for on-board battery charging, which achieves above 96% efficiency and 37 W/in^3.

Despite good performances at high switching frequency for TCM, a major drawback of TCM-based converters is its wide switching frequency range, which changes as a function of line cycle and load. The huge variation yields excessive turn-OFF switching loss, as well as excessive core and winding losses of the inductor, especially at light loads. Moreover, the related switching frequency is very easy to become extremely high when inappropriate electrical parameters are applied in TCM-based converters. Taking the 1.2-kW megahertz PFC in [16] as an example, the calculated switching frequency variation is 1–3 MHz.

When the PFC inductor value is just decreased from 10 to 8 μH, the new switching frequency variation can be calculated as 2–6 MHz. Due to the doubled switching frequency, losses of GaN HEMTs and the inductor become larger and will result in a significant reduction in overall efficiency. In addition, the doubled switching frequency will increase the burden of the driver circuits, including higher power dissipation, significant driver delays at higher switching frequency. Similarly, smaller control cycles in the digital control for TCM are also required at this time, which makes it difficult to implement. It can be seen that the circuit parameter design of the TCM converter will become harsher at high switching frequency and limit the feasibility of TCM control in turn.

In pervious works, several ideas are proposed to restrict the huge switching frequency variation in TCM. A discontinuous conduction mode (DCM) operation for switching frequency limitation is applied in a DCM/CCM boundary boost PFC converter [18]. The PFC operates at critical conduction mode (CRM) normally. When the switching frequency exceeds the allowed frequency, PFC will change to constant frequency DCM mode. With the simple DCM operation, the higher switching frequency generated by pure CRM mode can be limited. However, valley switching or non-ZVS will generate during DCM operation, which will lead to higher switching losses. Literature [19] proposed a quasi-constant frequency triangular current modulation (QCFTCM) technique to overcome the frequency variation in TCM. The quasi-constant switching frequency is implemented by increasing the desired negative inductor current. ZVS can also be achieved due to larger negative current, but the increased current ripple will lead to higher conduction losses in GaN HEMTs. In some cases, there is a significant drop in efficiency. In this article, both DCM and QCFTCM operations in H-bridge inverter are discussed in details. According to respective control implementation and losses distribution in DCM and QCFTCM, a hybrid TCM control method is proposed for good tradeoff. In order to make a good tradeoff between the switching frequency variation and efficiency in TCM-based inverters, an exact loss evaluation should be executed. Therefore, an improved analytical loss model for GaN HEMTs considering nonlinear junction capacitance as well as an accurate analytical inductor loss model is proposed for this reason. Based on the above models, an optimization algorithm is established for optimizing the performances of the hybrid TCM control. According to the final experimental results, compared with the TCM control, the optimal hybrid control has smaller switching frequency variation and higher efficiency, which is verified in the final experimental results.

The rest of this article is organized as follows. In Section II, the basic operation of TCM control in the H-bridge inverter is presented, while the related variation of switching frequency is also analyzed through derived formulas considering resonant transition. In Section III, the hybrid TCM control method is proposed and discussed in detail. In Section IV, the detailed loss modeling for GaN HEMTs and inductors in TCM-based inverters are presented. The related optimization algorithm is established for optimizing the performances of the hybrid TCM control is given in Section V. Finally, the proposed hybrid TCM control is verified in an interleaved GaN-based megahertz single-phase inverter. Corresponding experimental results are shown in Section VI.

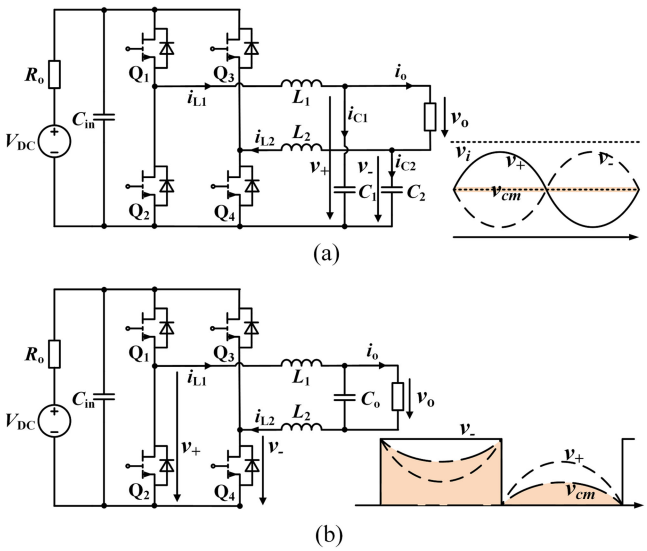

Fig. 1. (a) Symmetrical PWM full-bridge topology with dual-buck configuration. (b) Symmetrical full-bridge topology with PWM + unfolder modulation.

II. TCM Basic Operation and Switching Frequency Variation Analysis in H-Bridge Inverter

A. Basic Operation

Fig. 1 shows two typical modulation strategies for full-bridge inverters. One is the symmetric PWM (SP) modulation shown in Fig. 1(a), the other is PWM + unfolder (PU) modulation in Fig. 1(b). TCM control can be applied in both topologies to achieve zero voltage turn-ON (ZVS), but the resonant transition in TCM control is different from each other. Therefore, the TCM basic operation in two different modulations should be discussed separately.

First, the basic operation of TCM control is presented under the SP mode topology. The simplified waveform of I_{L1}, v_{ds1} and gate signal in TCM operation is depicted in Fig. 2(a). One switching cycle when the output voltage $v_o>0$ is divided into five intervals shown as follows:

Interval 1 (t_1–t_2)*:* The related transient state is shown in Fig. 2(b). The switches Q_1 and Q_4 are turned ON at t_1. Soon after the inductor currents I_{L1} and I_{L2} rise linearly for a fixed-on time (T_{on}). At the end of this interval, Q_1 and Q_4 are turned OFF and Interval 2 begins.

Interval 2 (t_2–t_3)*:* At the beginning of this interval, the output capacitors C_{OSS1} and C_{OSS4} start to be charged to input voltage V_{dc} while C_{OSS2} and C_{OSS3} are discharged at the same time. As shown in Fig. 2(c), the four output capacitors together with two inductors L_1, L_2 and two output stage capacitors C_1, C_2 form a resonance circuit. During the resonance transition, the inductor currents i_{L1} and i_{L2} continue to increase until both of the voltages across the switch Q_1 and Q_4 reaches V_{dc} and then decrease.

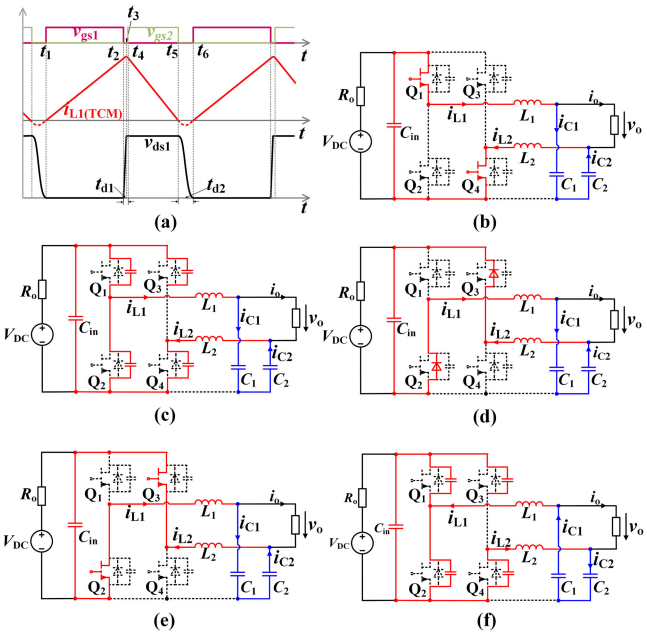

Fig. 2. (a) Key waveforms for TCM operation, and related TCM resonant transition in SP mode topology during (b) t_1–t_2, (c) t_2–t_3, (d) t_3–t_4, (e) t_4–t_5, and (f) t_5–t_6.

This interval can be described by solving a nonlinear differential equation

$$L_1\frac{d^2q_1(t)}{dt^2}+v_{Q1}(q_1(t),t)+L_2\frac{d^2q_4(t)}{dt^2}+v_{Q4}(q_4(t),t)=V_{dc}-v_o \tag{1}$$

where $q_1(t)$ and $q_4(t)$are the charges of C_{OSS1} and C_{OSS4}, respectively, and v_{Q1} and v_{Q2} are the voltages across C_{OSS1} and C_{OSS4}, respectively. Because the junction capacitors C_{OSS1} and C_{OSS4} are nonlinear during the charging process, the charges $q_1(t)$ and $q_4(t)$ cannot be expressed by exact formulas. Actually, (1) is very hard to be solved. For simplifying the above differential equation, the nonlinear junction capacitors can be replaced by constant effective output capacitance $C_{\mathrm{O(TR)}}$, which can be obtained in the related datasheet. Substituting $C_{\mathrm{O(TR)}}$ into (1), the simplified differential equation can be given as below:

$$L_1C_{O1(TR)}\frac{d^2v_{Q1}(t)}{dt^2}+v_{Q1}(t)+L_2C_{O4(TR)}\frac{d^2v_{Q4}(t)}{dt^2}+v_{Q4}(t)=V_{dc}-v_o. \tag{2}$$

Interval 3 (t_3–t_4)*:* This interval begins after capacitors C_{OSS1}, C_{OSS4} are charged to the input voltage V_{dc} and capacitors C_{OSS2}, C_{OSS3} is discharged to zero. Due to the very short resonance period, the inductor currents I_{L1} and I_{L2} start to commutates the body diode of Q_2 and Q_3, respectively, during the rest of dead time td1, which is shown in Fig. 2(d). Before the interval 4 begins, the voltages across switches Q_2 and Q_3 are always embedded in zero voltage.

Interval 4 (t_4–t_5)*:* When the gate voltages v_{gs2} and v_{gs3} become high level, the interval 4 starts. Both switches Q_2 and Q_3 can be turned-ON at zero voltage at t_4. After that, the inductor currents decrease linearly because the voltages v_{L1} and v_{L2} across both inductors are negative. The current flow loop is shown in Fig. 2(e).

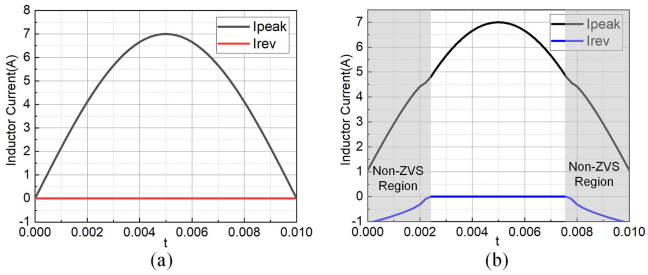

Fig. 3. Envelope of inductor current in TCM control for (a) SP mode topology, (b) PU mode topology.

Interval 5 (t_5–t_6)*:* Once inductor currents i_{L1} and i_{L2} reach zero, Q_2 and Q_3 are turned OFF and the interval 5 begins. As shown in Fig. 2(f), inductors L_1, L_2 and the output capacitors of four switches form a resonant circuit, which is the same as that in interval 2. In this resonant loop, the behavior is mainly depended on the output stage capacitor voltages v_{C1}, v_{C2}. During the positive cycle, v_{C1} always exceeds the half of the input voltage V_{DC} and v_{C2} is less than half of the input voltage V_{DC}. Therefore, both of the voltages across the switch Q_1 and Q_4 can reach zero voltage during the resonance. ZVS of Q_1 and Q_2 can finally be achieved at the turn-ON instant.

Fig. 3(a) shows the desired envelope of inductor current to achieve ZVS when TCM is applied in the SP mode topology. There is no non-ZVS region during the line cycle. It can be concluded that full-ZVS of this topology can be achieved without extra ZVS extension proposed in [16]. As for the PU mode topology, the TCM operation is slightly different from that in the SP mode. Considering a reversed power conversion, this topology actually corresponds to the totem-pole PFC rectifier. Therefore, the related TCM operation is also similar with that in the totem-pole PFC. However, there is one issue that the non-ZVS region is different for rectifier mode and inverter mode. According to the principle of symmetry, the non-ZVS region is complementary between rectifier mode and inverter mode. In other words, extra negative current or ZVS extension is needed in inverter mode when the output voltage V_o is less than the input voltage V_{dc}, which is shown in Fig. 3(b). The required extra negative current can be given as follows:

$$i_{neg}(t)=\begin{cases}-\sqrt{2\frac{q_c(t)}{L}(V_{dc}-2v_O(t))}, & \text{if } v_O(t)\le 0.5V_{dc}\\ 0, & \text{else}\end{cases} \tag{3}$$

where $q_c(t)$ is the charge of C_{OSS} during turning-OFF process. For simplifying the equation, the constant effective output capacitance $C_{\mathrm{O(TR)}}$ multiplied by the input voltage V_{dc} can replace $q_c(t)$. In addition, the simulated TCM inductor currents in both modulations are compared in Fig. 4. Considering the actual control implementation and guarantee for ZVS, both simulations slightly increase the negative current calculated by (3).

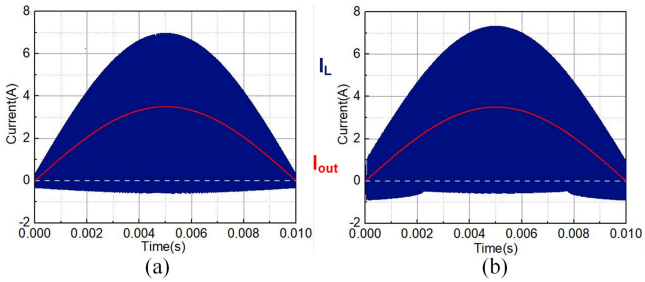

Fig. 4. Simulated inductor current in TCM control for; (a) SP mode topology; (b) PU mode topology.

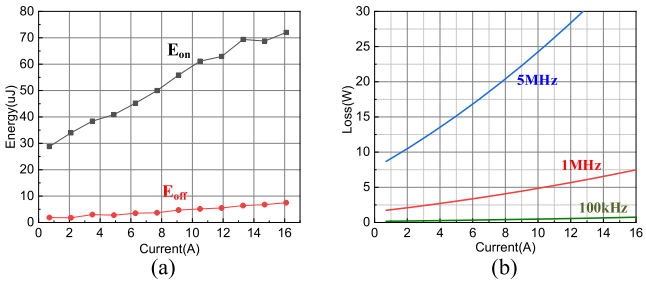

Fig. 5. (a) Measured $E_{\rm on}$ and $E_{\rm off}$ of a GaN device sample. (b) Related turn-OFF switching loss versus switching frequency.

B. Switching Frequency Variation

TCM control is a simple soft-switching technique without additional auxiliary circuits. It is feasible to achieve high power density without efficiency reduction by increasing the switching frequency directly. However, due to the inherent switching frequency variation of TCM, the TCM-based high frequency converter can easily achieve megahertz level even to dozens megahertz. Some issues will become more significant than low frequency conversion at this time. The first is the electromagnetic interference (EMI) problems. The EMI spectra of megahertz operation will become higher at high frequency [20], [22]. The radiated EMI also become significant due to the compact size for megahertz converter [23]. It leads to more complicated conducted EMI suppression at megahertz range. The second is the rare magnetic materials for high frequency conversion. For most magnetic cores in commercial, the related operating frequencies are usually below 5 MHz [24]–[26]. Once the frequency exceeds 5 MHz, the inductor will become very difficult to design. Meanwhile, the digital control of megahertz conversion is also a challenge. The limited processing speed in single DSP solution and the low resolution of digital PWM limits the converter performances at this time [27], [28]. The last but not least is the switching losses of semiconductors. Fig. 5(a) shows the switching loss distribution of one of GaN device samples. The switching loss is tested under double-pulse test setup discussed in [29]. As shown in Fig. 5(b), the turn-OFF switching loss of the measured GaN sample at 100 kHz is very small and nearly can be neglected compared with the conduction loss. Once pushing the switching frequency to megahertz range, the turn-OFF switching loss will become significant. Therefore, the variation of switching frequency in TCM control should be carefully managed to prevent the above problems generated by extremely high frequency.

TABLE I
MAIN INVERTER PARAMETERS FOR ANALYZING SWITCHING FREQUENCY VARIATION IN TCM CONTROL

Part.	Parameter	Value
Main Topology	Input voltage V_{dc}	400V
	Output voltage V_{orms}	220V
	Rated output power P_o	500W
	Output voltage frequency f_o	50Hz
	Output stage inductor value L	20uH
Selected Semiconductor	Effective junction capacitor value $C_{O(TR)}$ @ GaN sample from GaN Systems. Inc.	35pF

For a more intuitive analysis of the switching frequency variation in TCM control, the equations for precisely calculating the switching frequency in both topologies are, respectively, given as follows:

$$f_{sw(t),SP}(t) = \frac{{V_{dc}}^2 - v_o(t)^2}{8LV_{dc}\,|i_o(t)|} + \sqrt{2LC_{O(TR)}}\,(2\pi - \theta_p) \tag{4}$$

$$f_{sw(t),PU}(t) = \frac{|v_o(t)|\,V_{dc} - v_o(t)^2}{4L(|i_o(t)| + i_{neg}(t))V_{dc}} + \sqrt{2LC_{O(TR)}}\,(2\pi - \theta_1 - \theta_2) \tag{5}$$

where

$$\theta_p = \tan^{-1}\left(\sqrt{\frac{L}{2C_{O(TR)}}} \cdot \frac{4\,|i_o(t)|}{V_{dc} + |v_o(t)|}\right) \tag{6}$$

$$\theta_1 = \tan^{-1}\left(\sqrt{\frac{L}{2C_{O(TR)}}} \cdot \frac{2\,|i_o(t)| - i_{neg}(t)}{|v_o(t)|}\right) \tag{7}$$

$$\theta_2 = \tan^{-1}\left(\sqrt{\frac{L}{2C_{O(TR)}}} \cdot \frac{|i_{neg}(t)|}{|v_o(t)|}\right) \tag{8}$$

where v_o(t) and i_o(t) are the instantaneous value of output ac voltage and current, respectively. Both equations consist of two parts. One is the theoretical switching period, the other is the required resonant transition times derived from (1) and (2), which is always ignored under low-frequency conversion (<100 kHz). Once applied in higher frequency conversion, the second part will become quite large as the first one. Therefore, the complete calculated switching frequency is applied for a more precise estimation of the switching frequency variation in this article. The switching frequency variation is first investigated between two topologies and then discussed in-depth in terms of the impact of certain specific parameters. The detailed results are presented in Table I.

According to (4) and (5), the switching frequency variation at different load in both topologies can be depicted as Fig. 6. The related curves are based on a specific inverter. The related parameters are presented in Table I. As shown in Fig. 6(a), the switching frequency variation is very huge at rated power, where the lowest switching frequency $f_{\rm sw\_min}$ is only 266 kHz, but the highest switching frequency $f_{\rm sw\_max}$ is up to 5 MHz. Quite large power dissipation will generate when GaN HEMTs operate

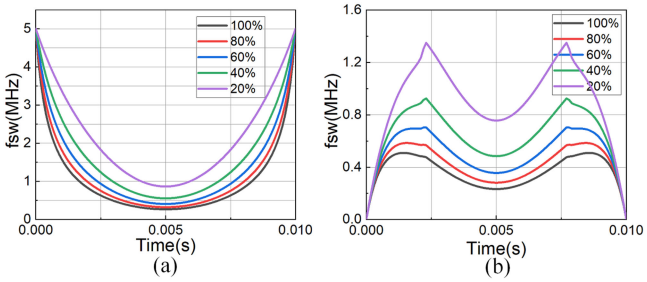

Fig. 6. Switching frequency variation during half line cycle at different load when TCM control applied in (a) SP mode topology; (b) PU mode topology.

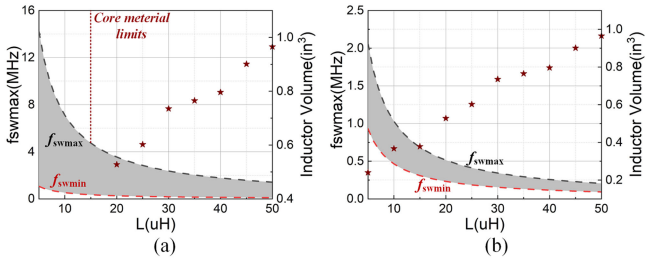

Fig. 7. Switching frequency variation range and designed inductor volume versus the output stage inductor value in (a) SP mode topology, (b) PU mode topology.

from several megahertz to a dozen megahertz ranges. $f_{\mathrm{sw\_min}}$ increases as the output power decreases while $f_{\mathrm{sw\_max}}$ maintains 5 MHz all the time. When the output power is below 20% of the rated power, $f_{\mathrm{sw\_min}}$ also achieves megahertz level. It can be known that the switching loss generated at light loads becomes so high that the efficiency will drop very badly, which loses the benefits of ZVS brought by the TCM control.

Similar variation of switching frequency in the PU mode topology can be seen in Fig. 6(b). The only difference from Fig. 6(a) is that the switching frequency will decrease to zero near the zero-crossing of ac current after reaching $f_{\mathrm{sw\_max}}$. Moreover, the switching frequency variation is smaller and $f_{\mathrm{sw\_max}}$ is much lower than the front one. It is clear that the performance of the PU mode topology will be better than the SP mode topology under the same load condition when TCM control is applied in both topologies.

On the other side, the switching variation will also have a significant impact on the pursuit of high power density. It is well known that the power density of power electronic converters is mainly contributed by the passive components especially the output stage inductors [30], [31]. For this reason, the power density of TCM-based converters is usually higher than the conventional hard-switching conversion with several hundred microhenry due to the designed smaller inductance value (usually dozens microhenry). However, the huge variation in TCM will lead to a restricted design for the inductance value L, thereby limit the power density. To illustrate this point intuitively, the switching variation range versus L in both topologies is presented in Fig. 7. By keeping the other parameters in Table I unchanged and only change the inductance value L, the switching variation range with different inductance values (5–50 μH) can be calculated according to (4) and (5). In addition, the designed inductor volume versus L is also given in Fig. 7.

Fig. 7(a) shows the switching frequency variation in the SP mode topology. As the inductance value L decreases from 50 to 5 μH, both $f_{\mathrm{sw\_max}}$ and $f_{\mathrm{sw\_min}}$ increase a lot, where $f_{\mathrm{sw\_max}}$ increases from 1.4 to 14 MHz and $f_{\mathrm{sw\_min}}$ increases from 100 kHz to 1 MHz. Though the inductor volume becomes smaller with lower inductor value L, the benefit will be limited by the extremely high switching frequency finally. Fig. 7(b) shows the switching frequency variation in the PU mode topology. Compared with Fig. 7(a), the switching frequency changes in a smaller range (below 2 MHz) and the inductor volume can achieve a smaller value. Higher efficiency and power density can achieve in this topology when both topologies have the same parameters.

In a conclusion, huge switching frequency variation is a significant problem in TCM control, especially in the SP mode topology. Excessive turn-OFF switching loss will reduce the efficiency of converters, which loses the benefits of ZVS. Although Increasing the inductance value can reduce the switching frequency, large variation still exists and low power density is obtained. This in turn will limit the pursuit of high-power density because small inductance value will lead to extremely high switching frequency. In TCM-based inverters, an effective method should be applied to achieve good tradeoff between efficiency and power density. And that is why the hybrid TCM control is proposed.

III. Hybrid TCM Control

A. Discontinuous Conduction Modulation (DCM)

Constant-switching frequency DCM is an effective method to eliminate the huge switching frequency variation. However, it will lead to extra non-ZVS problems when DCM is applied in these two topologies instead of TCM.

First, the simulated DCM inductor currents in both SP and PU modes are depicted in Fig. 8, where $f_{\mathrm{sw\_min}}$ of TCM is chosen for the switching frequency of DCM. It can be seen that the *LC* resonance still occurs after the inductor current decreases to zero. Different from TCM, the resonance will last for several cycles due to the long dead time t_{d2} in DCM. As is shown in Fig. 8(a), ZVS is only achieved when the dead time t_{d2} is equal to $(0.5+n)T_0$ $(n \in N)$. During the line cycle, some switching points may not match the above equation and located in the partial hard-switching (p.h.) region indicated in Fig. 8(a). Due to the voltage v_{ds} in p.h. region is not equal to zero, hard-switching-ON occurs and results in higher switching-ON losses.

As for the DCM operation in the PU mode, Fig. 8(b) shows that valley switching (VS) will substitute ZVS when the output voltage is lower than half of the dc bus voltage. Due to extra valley-switching losses, the total partial switching losses will become higher.

Accordingly, the partial hard-switching-ON energy in both inverter modes can be calculated as follows:

$$E_{p.h.(SP)}(t) = 0.25 \cdot C_{OSS}[V_{dc} - \sqrt{2}V_o \sin\omega t + (V_{dc} + \sqrt{2}V_o \sin\omega t) \cdot \cos(\omega_0(t_d \bmod T_0))]^2 \quad (9)$$

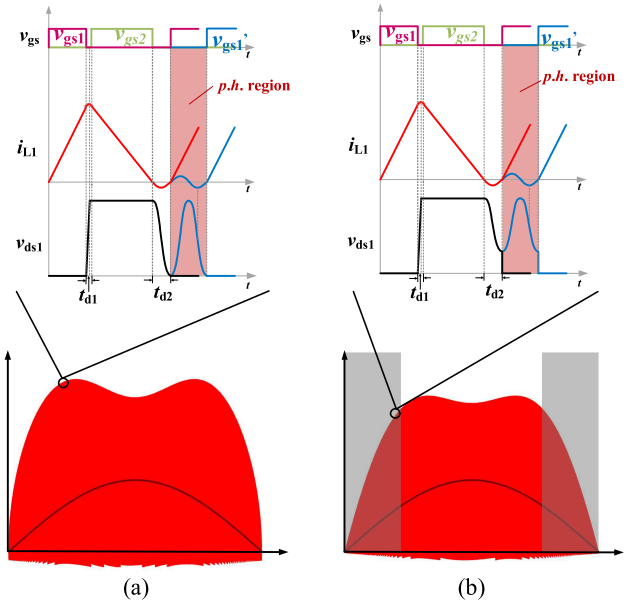

Fig. 8. Simulated inductor DCM currents along with key switching waveforms of DCM operation in: (a) SP mode; (b) PU mode.

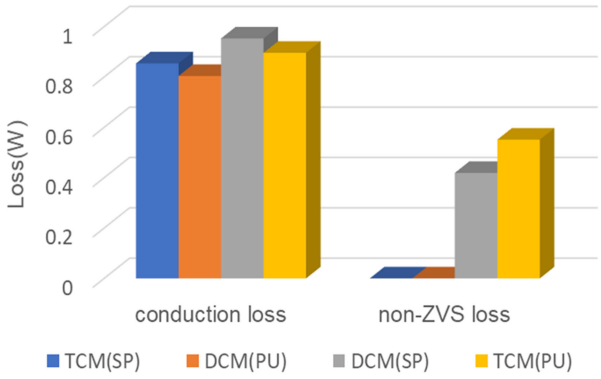

Fig. 9. Loss comparison for TCM(SP), TCM(PU), DCM(SP) and DCM(PU).

$$E_{p.h.(PU)}(t) = 0.5C_{OSS}(V_{dc} + \sqrt{2}V_o \sin\omega t(\cos(\omega_0(t_d \bmod T_0)) - 1)^2 \tag{10}$$

with

$$\omega_0 = \frac{1}{\sqrt{2LC_{OSS}}} \tag{11}$$

where T_0 is the LC resonant period, and $t_{\rm d}$ is the required DCM dead time. By substituting parameter values in Table I into (9) and (10), the loss comparison including conduction loss and partial hard-switching loss is presented in Fig. 9. It can be known that DCM mode have higher conduction losses and extra partial hard-switching losses compared with TCM. Therefore, constant-switching frequency DCM is not a good choice.

On the other side, the DCM operation can also be implemented with ZVS or VS by adjusting the required dead time $t_{\rm d2}$. However, due to the short LC resonant period, ZVS or VS is very hard to maintain over a line cycle. Moreover, the VS loss is still significant in the total converter loss. According to literature

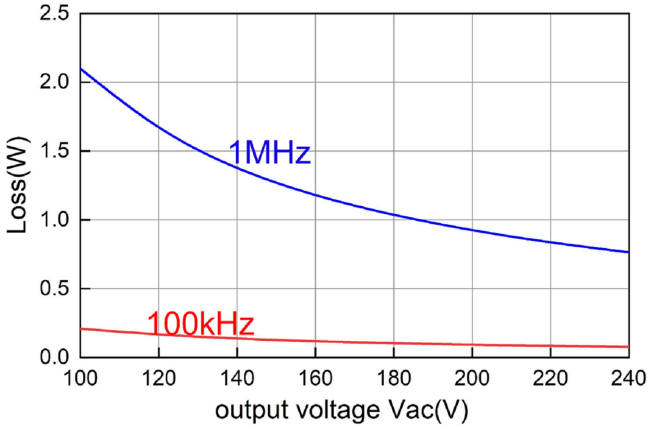

Fig. 10. Line-cycle averaged valley-switching loss versus output voltage.

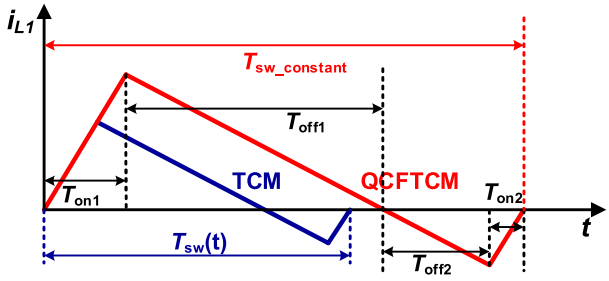

Fig. 11. Inductor current for one switching cycle in TCM & QCFTCM.

[16], the VS losses can be derived below

$$E_{vs}(V_o, t) = \begin{cases} 0.5C_{OSS}(V_{dc} - 2\sqrt{2}V_o \sin\omega t)^2, & (V_o \le 0.5V_{dc}) \\ 0, & (V_o > 0.5V_{dc}). \end{cases} \tag{12}$$

When the switching frequency is pushed to the megahertz level, the related VS losses will become dominant and result in low efficiency, as shown in Fig. 10.

B. Quasi-Constant Frequency TCM (QCFTCM)

Except for DCM, another derived-TCM modulation can also be used for eliminating the switching frequency variation. The derived-TCM modulation is called as quasi-constant frequency triangle current modulation (QCFTCM). The basic idea of QCFTCM is to maintain almost fixed switching frequency during the line cycle [19].

First of all, the minimum switching frequency $f_{\rm sw\_min}$ of TCM is chosen for the switching frequency of QCFTCM. Then, the switching frequency, which originally exceed $f_{\rm sw\_min}$ in TCM, can be kept in $f_{\rm sw\_min}$ just by increasing the desired negative current. Correspondingly, the peak current has to be increased in order to maintain the same average current as shown in Fig. 11. The control implementation of QCFTCM is similar to TCM. In TCM, the auxiliary switch is turned OFF after the current reaches zero or after a programmable time delay for ZVS. In QCFTCM, zero current is detected and after ZCD a variable delay of $T_{\rm off2}$ is given to turn OFF the auxiliary switch. It is known that full ZVS

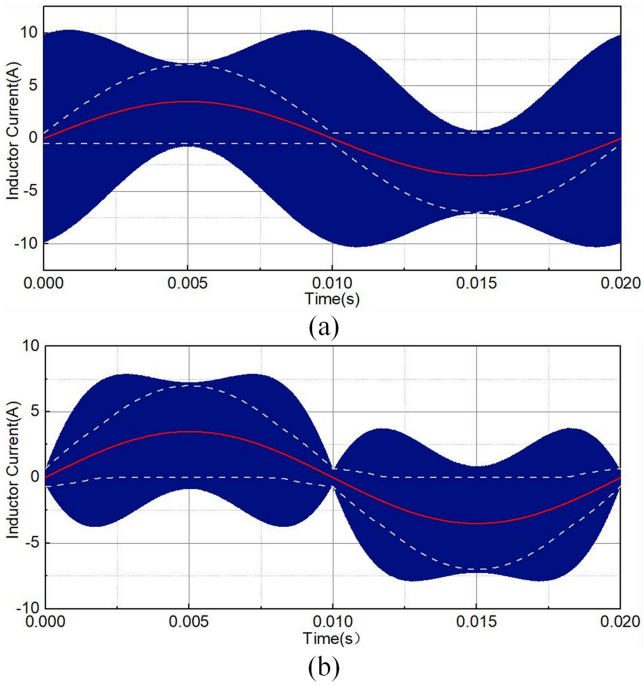

Fig. 12. Simulated Inductor current for one switching cycle in QCFTCM.

can also be achieved in QCFTCM due to the higher negative current compared with TCM.

According to the control trajectory, the required extra conduction time is calculated with (9) in order to maintain the same switching frequency. The related negative current in QCFTCM is also calculated as (10)

$$T_{off2}(t) = \begin{cases} \frac{1}{2}\left(\frac{1}{2f_{sw}} - \frac{4L\cdot|i_o(t)|}{V_{dc}-|v_o(t)|}\right) - \frac{|v_o(t)|}{4f_{sw}\cdot V_{dc}} & , \text{(SP)} \\ -\frac{2L\cdot {V_{orms}}^2}{P_o} + \frac{V_{dc}-|v_o(t)|}{2f_{sw}\cdot V_{dc}} & , \text{(PU)} \end{cases} \tag{13}$$

$$I_{neg\_qcftcm}(t) = \begin{cases} \frac{V_{dc}-v_o(t)}{2L}T_{off2} & , \text{(SP)} \\ \frac{v_o(t)}{2L}T_{off2} & , \text{(PU)} \end{cases} \tag{14}$$

where f_{sw} is the selected switching frequency for QCFTCM and P_o is the output power of the inverter.

To further investigate this derived-TCM control method, Fig. 12 shows simulated QCFTCM inductor currents in both topologies. It can be seen that current ripples in both topologies become larger than that in TCM after QCFTCM operation, especially at SP mode. As shown in Fig. 12(a), the current ripple in the SP mode reaches maximum near the zero-crossing of the output current.

The semiconductor conduction losses in both topologies with TCM and QCFTCM are also calculated and compared in Fig. 13. In the SP mode topology, conduction loss increases from 0.8 to 2 W after the QCFTCM operation. In the PU mode topology, conduction loss in QCFTCM increases from 0.9 to 1.1 W. It can be inferred that the increased conduction losses will directly lead to lower efficiency. Moreover, the larger current ripple will also cause higher inductor loss as well as higher DM noise. The former will lead to further reduction in efficiency, while the latter

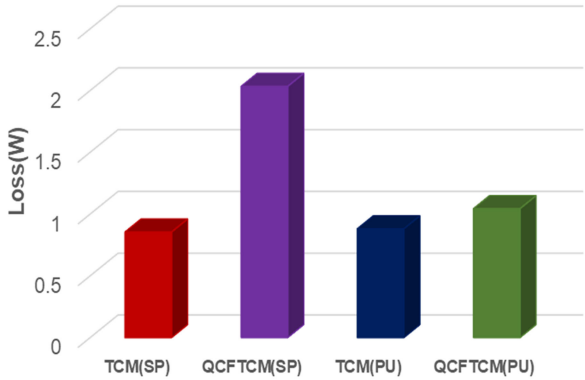

Fig. 13. Conduction loss comparison for TCM (SP mode), TCM (PU mode), QCFTCM (SP mode), and QCFTCM (PU mode).

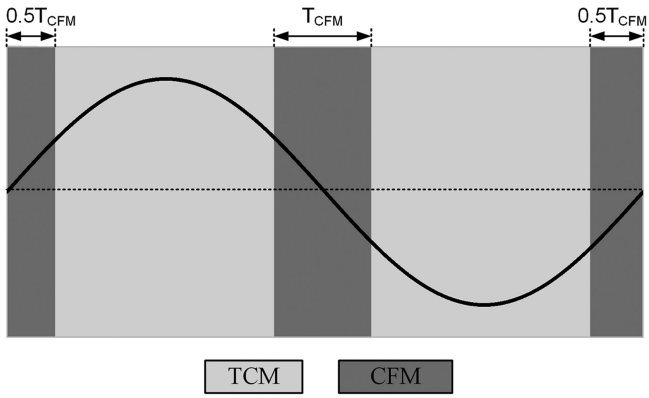

Fig. 14. Line cycle operation for hybrid TCM control.

will lead to lower power density due to larger volume for DM filter. Though the variation of switching frequency is eliminated by QCFTCM, more issues are introduced.

C. Conception of Hybrid Control Method

According to the aforementioned analysis, both DCM and QCFTCM are effective solutions for eliminating huge switching frequency but not a qualified candidate for achieving high efficiency and high power density. In order to narrow the switching frequency variation while improving the efficiency in TCM-based converters as much as possible, the hybrid TCM control is proposed in this section.

It is worth noting that the variation of switching frequency in TCM is based on the circuit parameters and operation condition. As shown in Fig. 15(a), the switching frequency increases relatively slowly around one quarter line cycle while increases very fast near the zero-crossing of output current. Most of the switching frequencies near the zero-crossing point exceed the megahertz, which are main contributors to switching-OFF losses. If these higher switching frequency sections in TCM can be replaced by those two constant frequency modulations (CFM), the huge switching variation as well as excessive switching-OFF loss can be reduced at the expense of less current ripple. The basic idea of hybrid TCM control lies behind combining TCM with CFM. Fig. 14 shows the intuitive operation mode over a line cycle.

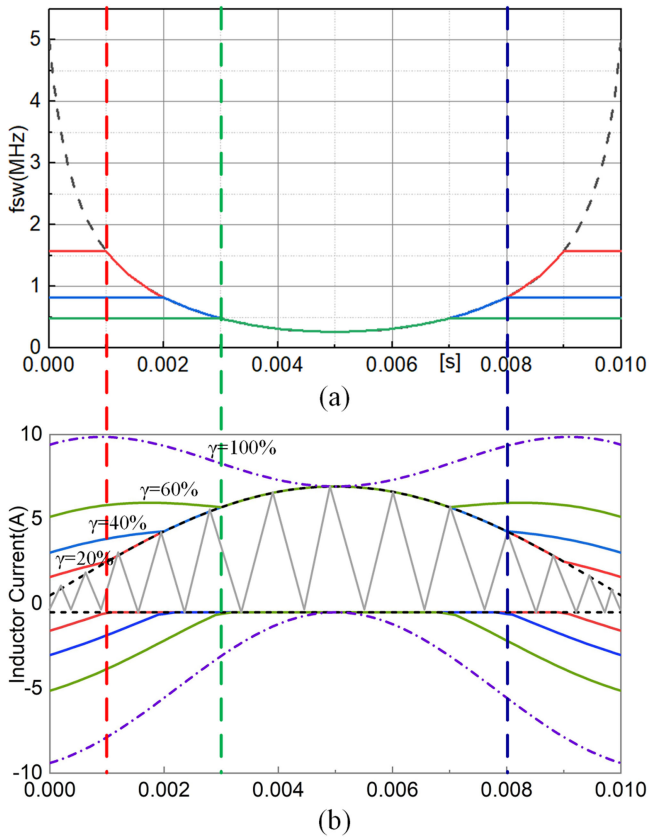

Fig. 15. (a) Switching frequency variation in hybrid TCM control under different QCFTCM operating intervals. (b) Inductor current shape under different QCFTCM operating intervals.

When DCM is applied for CFM, the resulting non-ZVS losses will become significantly high at high frequency and then worsen the related performance. In contrast, QCFTCM can achieve ZVS just at the cost of slightly higher conduction losses. Therefore, the proposed hybrid TCM control is focused on TCM + QCFTCM in this article.

A symmetrical interval is added at every output current zero-crossing point for the QCFTCM operation. For ease of description, γ is put forward to represent the actual QCFTCM operation interval. The ratio γ is defined as

$$\gamma = \frac{2T_{QCFTCM}}{T_{\text{line}}}. \tag{15}$$

With different value for γ ($0 < \gamma < 1$), the switching frequency variation can be adjusted as needed. Fig. 15 shows the switching frequency and related inductor current ripple with different γ.

Moreover, due to the similar control idea of QCFTCM and TCM, the proposed hybrid TCM can easily apply the control block diagram of TCM with partial modification. The control scheme for hybrid TCM control in the SP mode inverter is presented in Fig. 16. The average current loop controls the average current to track desired sinusoidal reference, which is the same as [32]. While the programmed extra OFF-time control is slightly different. When the current is running into the QCFTCM interval, the reference current should be added to

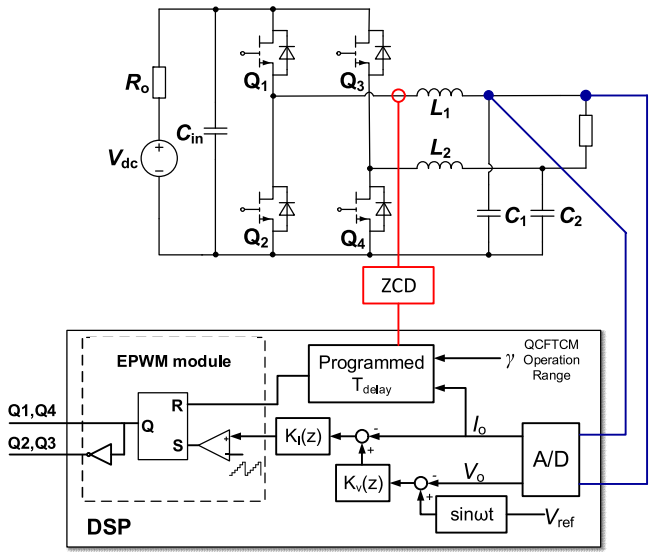

Fig. 16. Control scheme for proposed hybrid TCM control in SP mode inverter.

the programmed extra OFF-time block to achieve the needed off time in QCFTCM and γ is the default value.

The detailed description for the hybrid TCM is all presented above. However, when applied in both SP and PU mode inverters, the QCFTCM operation interval γ should be investigated more deeply. γ has a flexible range of values as mentioned above. When the value of γ is too large (>0.9), the dominated current ripple also leads to excessive conduction losses just like pure QCFTCM. When the value of γ is too small, the very short interval will still result in quite large variation of switching frequency.

Therefore, in order to determine the optimal γ for best performance, an optimization algorithm is established. The optimization algorithm is based on loss estimation including GaN HMETs losses and inductors losses. In Section IV, the GaN HEMTs and inductors analytical loss models are proposed and described in detail. The final optimization process is presented in Section V.

IV. Loss Modeling for GaN HEMTs and Inductor in TCM Control

A. GaN HEMTs Analytical Loss Model

Subsection I. Turn-OFF Transient Model: Estimating the switching loss of GaN HEMTs accurately is a challenge. Among all the methods proposed so far, LTspice simulation is a widely used method to estimate the related behavior. However, the simulation results depend on the accuracy of the Spice model given by the manufacturer, which differs from each other. For better estimation of GaN HEMTs' losses, several analytical models, which divided the switching transient into several subperiod and used piecewise linearization for approximate calculation, are proposed [33], [34]. Most models proposed earlier have not considered the nonlinear characteristics of the device capacitance and the nonlinear transfer characteristic, which can affect the accuracy of calculation results. Recently, more accurate transient

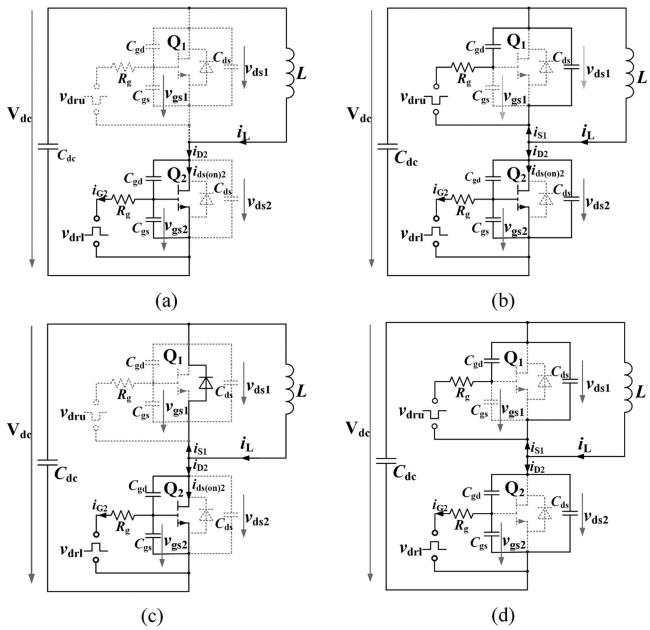

Fig. 17. Equivalent circuits for turn-OFF transient process of GaN HEMTs: (a) gate delay subperiod; (b) voltage rise subperiod; (c) current fall subperiod; (d) COSS charge subperiod.

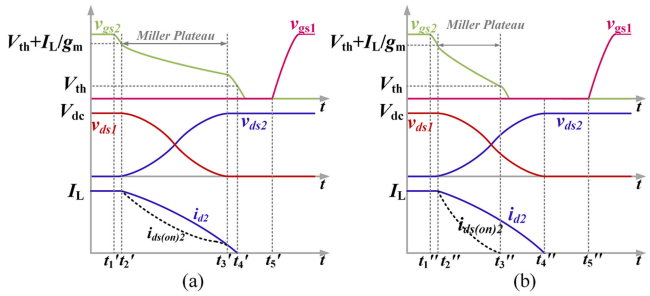

Fig. 18. Related turn-off transient waveforms at (a) normal current fall mode; (b) C_{OSS} charge mode.

models with nonlinear junction capacitors have been proposed in [35] for Si and SiC MOSFET. However, due to ultralow reverse transfer capacitance $C_{\rm rss}$, the aforementioned model is inappropriate for GaN HEMTs. And thus, a well-matched turn-OFF model for GaN HEMT based on [35] is proposed in this section. The related turn-OFF equivalent circuit and transient waveforms are depicted in Figs. 17 and 18. The parasitic inductance is ignored for a concise description. The details of transient subperiods are as following.

1) Subperiod1(t_1'–t_2') (Turn-OFF Delay): At t_1, turn-OFF signal is coming and gate–source voltage v_{gs2} begins to fall from V_{drh} as expressed by (16). This interval ends at t_2 when v_{gs2} falls to $(V_{th} + I_L/\, g_m)$, where g_m is the transconductance and V_{th} is the threshold voltage

$$R_g \cdot C_{iss} \frac{dv_{gs2}}{dt} + v_{gs2} = v_{drl}. \tag{16}$$

2) Subperiod2(t_2'–t_3') (Voltage Rise and Current Fall): After t_2', the drain to source on current $i_{\rm ds(on)2}$ begins to fall. Meanwhile, C_{ds1} is charged from v_{dson} by i_{cds1}. Equations (17)–(19) can be derived to express this period

$$C_{gs}(v_{ds2}) \cdot \frac{dv_{gs2}}{dt} + C_{gd}(v_{ds1}) \cdot \frac{dv_{gd2}}{dt} = -\frac{v_{gs2} - V_{drl}}{R_g} \tag{17}$$

$$(C_{oss}(v_{ds1}) + C_{oss}(v_{ds2}))\frac{dv_{ds2}}{dt} + g_m(v_{gs2} - V_{th}) = i_L \tag{18}$$

$$v_{ds2} + L\frac{di_L}{dt} = V_{dc} \tag{19}$$

where $C_{oss} = C_{ds} + C_{gd}$. The state equation (A1) can be derived from the above equations

$$\begin{bmatrix} \dot{v}_{gs1} \\ \dot{v}_{ds1} \\ \dot{I}_L \end{bmatrix} = \begin{bmatrix} -(a + g_m \cdot b) & 0 & b \\ -g_m \cdot c & 0 & c \\ 0 & -d & 0 \end{bmatrix} \begin{bmatrix} v_{gs1} \\ v_{ds1} \\ I_L \end{bmatrix} + \begin{bmatrix} a \cdot V_{drl} + b \cdot g_m \cdot V_{th} \\ c \cdot g_m \cdot V_{th} \\ d \cdot V_{DC} \end{bmatrix} \tag{20}$$

where $a = \frac{1}{R_g C_{iss}}$, $b = \frac{C_{gd}}{C_{iss}(C_{oss1}+C_{oss2})}$, $c = \frac{1}{C_{oss1}+C_{oss2}}$, $d = \frac{1}{L}$.

3) Subperiod3(t_3'–t_4') (Current Fall): Once v_{ds2} has been charged to V_{dc}, Q_2 begins to conduct reversely. Because v_{ds1} is clamped to V_{DC} by Q_2, $dv_{ds1}/dt = 0$. Equation (13) is presented to describe this interval. Current fall period ends when v_{gs} falls to V_{th} to block the channel of Q_1

$$R_g \cdot C_{iss} \frac{dv_{gs2}}{dt} + v_{gs2} = v_{drl}. \tag{21}$$

A typical turn-OFF transient model for GaN HEMTs is depicted above according to the literature [35]. However, the model derived from SiC MOSFETs is not suitable for all working conditions in GaN HEMTs. According to some experimental results for GaN HEMT [21], the miller plateau disappears very quickly and would not last until $v_{\rm ds}$ charge to $V_{\rm dc}$ when the drain current is small. A boundary current $I_{\rm B}$ can be calculated as (22) according to differential equations in subperiod2

$$I_B = \frac{\beta(V_{th} - V_{drl})}{R_g(R_g \cdot g_m - \beta)} \tag{22}$$

where $\beta = \frac{C_{OSS}(v_{ds(on)}) + C_{OSS}(V_{dc} - v_{ds(on)})}{C_{gd}(v_{ds(on)})}$.

When the load current is below $I_{\rm B}$, $i_{\rm ds(on)}$ drops to zero quickly while the voltage $V_{\rm ds2}$ still rising. As shown in Fig. 18(b), a new subperiod will appear instead of subperiod3. The related behavior is shown in Fig. 17(d) and detailed description is given below.

4) Subperiod4(t_3''–t_4'') (C_{OSS} Charge): At the beginning, the channel of Q_2 has been blocked. Therefore, $I_{\rm L}$ is used to charge $C_{\rm OSS1}$ and $C_{\rm OSS2}$. Equation (23) is derived to present $v_{\rm ds1}$. $C_{\rm OSS}$ charge period ends when vds1 is charged to $V_{\rm dc}$

$$L(C_{oss}(v_{ds1}) + C_{oss}(v_{ds2}))\frac{d^2v_{ds2}}{dt^2} + v_{ds2} = V_{dc}. \tag{23}$$

So far, a complete description of GaN HEMTs turn-OFF transition is given above. Once given the initial variables, such

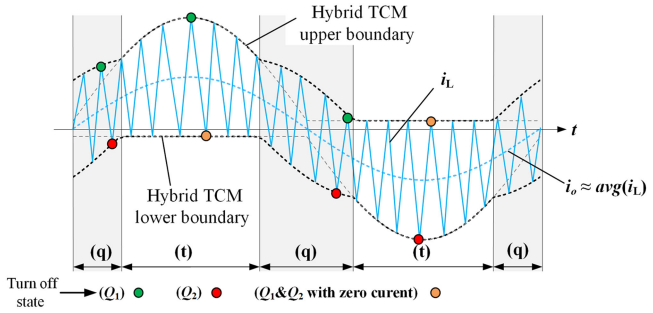

Fig. 19. Turn-off state of single switch over a line cycle (SP mode). Positive half cycle: when the status is in QCFTCM operation (q), Q_1 is turned OFF at peak current (PC) while Q_2 at reverse current (RC); when the status is in TCM operation (t), Q_1 at PC & Q_2 at zero current (ZC). Negative half cycle: when the status is in QCFTCM, Q_1 at RC & Q_2 at PC; when the status is in TCM, Q_1 at ZC & Q_2 at PC.

as $v_{\rm gs}$, $v_{\rm ds}$, $i_{\rm load}$, $V_{\rm dc}$, the needed curves for loss estimation can be obtained by solving those differential equations iteratively. And then the switching energy during one turn-OFF period can be given as

$$E_{off}(i_{\rm load}) = \int_{t_1'}^{t_4'} v_{ds}(i_{\rm load}, t') \cdot i_{ds(on)}(i_{\rm load}, t') dt' \quad (24)$$

by repeating the above calculation at different load currents, the turn-OFF loss at different load currents $E_{off}(I_{\rm load})$ can be obtained.

Subsection II. Soft Switching Turn-OFF Loss Model: For calculating the exact soft switching losses in TCM or TCM derived modulation, the related turn-OFF status of each GaN HEMTs should be investigated. Fig. 19 shows the turn-OFF state of hybrid TCM for SP mode over a line cycle. It can be seen that Q_1 is always turned OFF at the upper boundary and Q_2 is turned OFF at the lower boundary. The turn OFF state of Q_1 and Q_2 is complementary between positive and negative line cycle. For simplifying and unifying the loss calculation, Q_1 and Q_2 can be seen as being turned OFF at both boundaries over half line cycle. After the modification, the switching losses during one switching cycle for TCM and QCFTCM section can be calculated, respectively

$$P_{off(t)}(I_{\rm load}, t) = E_{off}(2\sqrt{2} I_{\rm load} \sin \omega t) \cdot f_{sw}(I_{\rm load}, t) \quad (25)$$

$$P_{off(q)}(I_{\rm load}, t) = \left[E_{off}(i_{\rm peak(q)}(t)) + E_{off}(i_{neg(q)}(t))\right] \cdot f_{sw}(I_{\rm load}, \frac{\gamma T_{\rm line}}{4}). \quad (26)$$

The final step is to average the line-cycles, so that the line-cycle averaged turn-OFF loss at different load currents ($\propto P_o$) for this hybrid TCM control is calculated according to

$$P_{off\_ave(h)}(I_{\rm load}) = \frac{1}{T_{\rm line}} \int_{\frac{\gamma T_{\rm line}}{4}}^{\frac{T_{\rm line}}{2} - \frac{\gamma T_{\rm line}}{4}} \times E_{off}(2\sqrt{2} I_{\rm load} \sin \omega t) \cdot f_{sw}(I_{\rm load}, t) dt$$

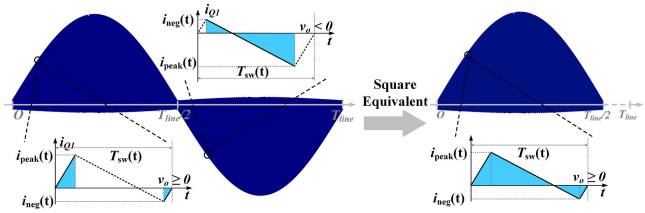

Fig. 20. Complementarity of Q_1 conduction region between positive and negative line cycle. On the basis of the energy equivalent, the conduction current can be equivalent to a half-wave current over the line cycle.

$$+ 2\frac{1}{T_{\rm line}} f_{sw}(I_{\rm load}, \frac{\gamma T_{\rm line}}{4}) \cdot \int_0^{\frac{\gamma T_{\rm line}}{4}} \left[E_{off}(i_{\rm peak(q)}(t)) + E_{off}(i_{neg(q)}(t))\right] dt \quad (27)$$

where γ is the QCFTCM ratio. When γ is equal to zero, the turn-OFF loss for TCM control can also be obtained.

Subsection III. Conduction loss model: The conduction loss can be easily calculated by RI^2 equation. $R_{\rm ds(on)}$ can be obtained through Datasheet. The key is to figure out the square of conduction current ${I_{\rm conduction}}^2$.

Fig. 20 shows the detailed conduction region of Q_1 over a line cycle. According to the principle of root mean square equivalence, the conduction current can be equivalent to half-wave inductor current. Similar with the calculation of switching loss, the line-cycle averaged conduction loss for hybrid TCM control can be calculated as follows:

$$P_{con\_ave}(I_{\rm load}) = \frac{1}{T_{\rm line}} \int_{\frac{\gamma T_{\rm line}}{4}}^{\frac{T_{\rm line}}{2} - \frac{\gamma T_{\rm line}}{4}} R_{ds(on)} \cdot I_{L(t)}^2(I_{\rm load}, t) \cdot f_{sw(t)}(I_{\rm load}, t) dt + \frac{2}{T_{\rm line}} f_{sw(t)}\left(I_{\rm load}, \frac{\gamma T_{\rm line}}{4}\right) \cdot \int_0^{\frac{\gamma T_{\rm line}}{4}} R_{ds(on)} \cdot I_{L(q)}^2(I_{\rm load}, t) dt \quad (28)$$

where $i_{L(t)}^2(t)$ and $i_{L(q)}^2(t)$are the square of conduction current during one switching cycle in TCM and QCFTCM, respectively. When γ is equal to zero, the conduction loss for TCM control can also be obtained.

B. Inductor Loss Model

Subsection I. Core Loss Model: For the given TCM-based application, the material is excited by a LF 50 Hz (ideally) sinusoidal voltage and superimposed HF square-wave voltage pulses. Therefore, on the one hand, the core loss model comprises a LF component where the generalized Steinmetz equation (GSE) is used

$$P_{c,LF} = V_c \cdot k \cdot f_{\rm line}^{\alpha} \cdot \hat{B}^{\beta} \quad (29)$$

where k, α, and β are the related core parameters for Steinmetz calculation.

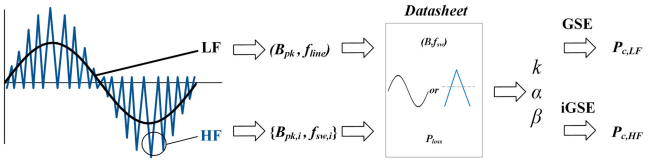

Fig. 21. Core loss calculation flow chart based on TCM waveforms.

On the other hand, the HF component may be calculated by the improved generalized Steinmetz equation (i^{2}GSE) for square-wave excitations proposed in [36]. The proposed core loss model considers the influence of the premagnetization H_{DC} and achieves high accuracy. However, the above core loss model is built on the premise of extra core loss measurements for different operating points. So far only the materials N87 and 2605SA1 mentioned in [36] are measured further and available for this core loss model. In a conclusion, this complete core model is mainly limited by the preliminary measurements and inappropriate for the given TCM-based application.

Fortunately, the extensive measurements in [37] show that not all materials losses vary under dc bias conditions. Among most magnetic cores for power conversion, powder core materials, such as KoolMu, iron, are confirmed to be premagnetization-independent. Therefore, an accurate and universally applicable core loss model for powder core materials can be derived from i^{2}GSE, in which only Steinmetz parameters for sinusoidal excitation from the data sheet are required. The simplified Steinmetz equation can be given as

$$P_{c,HF} = V_c \frac{1}{T_{\text{line}}} \sum_i k_i \left| \frac{1}{T_i} \right|^{\alpha} (\Delta B)^{\beta-\alpha} \tag{30}$$

with

$$k_i = \frac{k}{(2\pi)^{\alpha-1} \int_0^{2\pi} |\cos\theta|^{\alpha} 2^{\beta-\alpha} d\theta}. \tag{31}$$

The parameters k, α, and β are Steinmetz parameters, which can be obtained from the data sheet. T_i are the corresponding time intervals of the piecewise linear HF flux segments ($\sum T_i = T_{\text{line}}$).

Fig. 21 illustrates the detailed core loss calculation process for TCM current waveforms. The detailed core loss calculation for both TCM and Hybrid TCM are given in the Appendix.

Subsection II. Winding Loss Model: The winding losses vary between different winding types. Considering the megahertz level frequency, litz or foil wire is the best candidate for inductor winding, which has low skin- and proximity-effect. However, an accurate analytical model for foil wire geometries is very complex due to the fact that 2-D approximation should be executed to achieve high accuracy. As for litz wires, well-known and tractable analytical models exist based on 1-D field approximations [38]. Therefore, only litz wire is considered and the related winding losses are calculated in this article.

In litz-wire windings, the total losses can be divided into skin-effect losses and proximity-effect losses. The skin-effect losses, including dc losses, of a litz-wire winding that consists of *n* strands, each with strand diameter di are calculated as

$$P_{W(S)} = n \cdot R_{DC} \cdot F_R(f) \cdot \left(\frac{\hat{I}}{n} \right)^2 \tag{32}$$

where R_{DC} is the dc resistance of one strand per unit length, and $F_R(f)$ can be found in [37].

The proximity-effect losses in litz-wire windings can also be calculated as

$$P_{W(P)} = n \cdot R_{DC} \cdot G_R(f) \left(\hat{H}_e^2 + \frac{\hat{I}^2}{2\pi^2 d_a^2} \right) \tag{33}$$

where d_a is the outer diameter of litz-wire, H_e is the external magnetic field strength, and $G_R(f)$ can be found in [37]. Since the selected core materials are always shaped into toroid, H_e can be neglected. The above equations can be simplified into

$$P_W = n \cdot R_{DC} \cdot \hat{I}^2 \cdot (F_R^*(f) + G_R^*(f)) \tag{34}$$

where $F_R^*(f) = \frac{F_R(f)}{n^2}$ and $G_R^*(f) = \frac{G_R(f)}{2\pi^2 d_a^2}$. With the similar calculation process, the line-cycle averaged winding losses for hybrid TCM control can be calculated as

$$\begin{aligned} &P_{w\_ave} \\ &= 2k \cdot \int_{\frac{\gamma T_{\text{line}}}{4}}^{\frac{T_{\text{line}}}{2} - \frac{\gamma T_{\text{line}}}{4}} \\ &\quad \times \frac{i_{L(t)}^2(t)[F_R^*(f_{sw(t)}(t)) + G_R^*(f_{sw(t)}(t))] f_{sw(t)}(t)}{T_{\text{line}}} dt \\ &\quad + 4k \left[F_R^* \left(f_{sw(t)} \left(\frac{\gamma T_{\text{line}}}{4} \right) \right) + G_R^* \left(f_{sw(t)} \left(\frac{\gamma T_{\text{line}}}{4} \right) \right) \right] \\ &\quad \cdot f_{sw(t)} \left(\frac{\gamma T_{\text{line}}}{4} \right) \cdot \int_0^{\frac{\gamma T_{\text{line}}}{4}} \frac{i_{L(t)}^2(t)}{T_{\text{line}}} dt \end{aligned} \tag{35}$$

where $k = N \cdot MLT \cdot n \cdot R_{DC}$. When γ is equal to zero, the conduction loss for TCM control can also be obtained.

V. Optimization Algorithm for Hybrid TCM Control

A. Optimization Algorithm

Based on the establishment of the above GaN HEMT loss and inductor loss models, an optimization algorithm is proposed in this article, which is shown in Fig. 22.

In the proposed optimization algorithm, all predesigned electrical parameters, i.e., the output inductor value *L*, are kept the same for both topologies. First, the initial parameter L_0 is determined while initial parameters f_{QCFTCM} and γ are iterated, and then the resulting current and voltage waveforms of each GaN HEMT and the resulting flux density of output inductor *L* can be calculated based on electrical model of the selected topology. Through the loss models proposed in Section IV, those calculated results can be transferred to single GaN HEMT loss and single inductor loss, respectively, which is then used to optimize total losses of the inverter. Finally, the optimal value γ can be determined based on the lowest losses.

Furthermore, due to the lower switching frequency of hybrid TCM control, the output inductor value *L* can also be selected

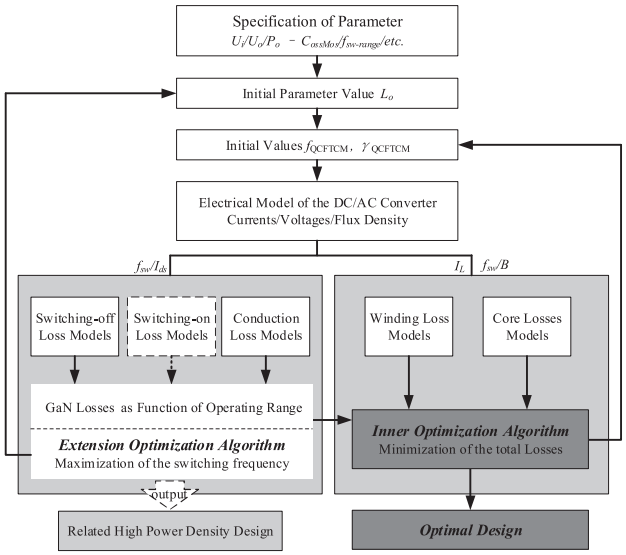

Fig. 22. Block diagram of the optimization procedure employed for maximizing the efficiency of the hybrid TCM control.

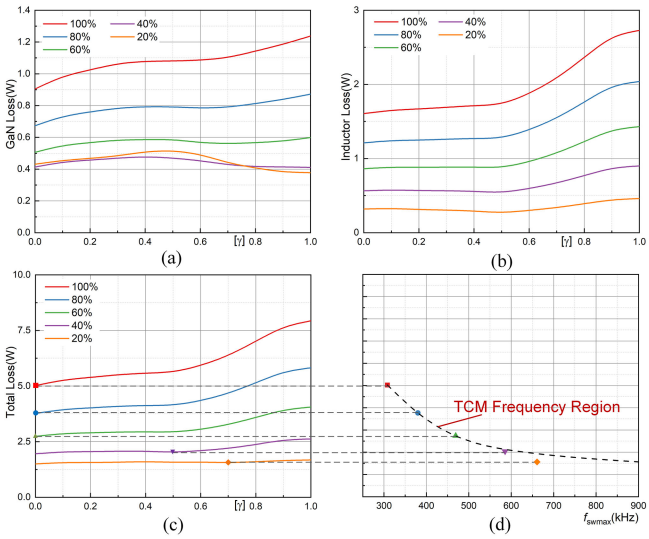

Fig. 23. (a) Calculated GaN HEMT loss versus QCFTCM ratio γ. (b) Calculated inductor loss versus QCFTCM ratio γ. (c) Total losses versus QCFTCM ratio γ. (d) Related highest switching frequency after optimization under different output power for PU mode inverter.

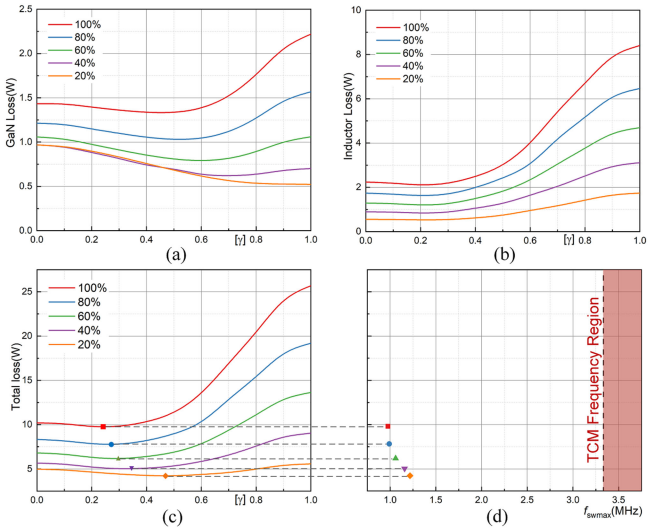

Fig. 24. (a) Calculated GaN HEMT loss versus QCFTCM ratio γ. (b) Calculated inductor loss versus QCFTCM ratio γ. (c) Total losses versus QCFTCM ratio γ. (d) Related highest switching frequency after optimization under different output power for SP mode inverter.

smaller, which can achieve higher power density than TCM. Therefore, another extension optimization algorithm for achieving higher power density can be executed. Therefore, the initial parameter L_0 is iterated in a certain range. The inner optimization algorithm is considered as an inner loop calculation at this time. It means the calculation should be run every iteration of L_0. After the data process, the switching frequency as well as the related losses versus the output inductor value can be obtained. According to the limits of switching frequency and power losses, the highest power density design can be determined finally.

B. Inner Optimization Results for Better Performance

The more detailed inner optimization process and results are given in this section. Related inverter parameters for this optimization are the same as shown in Table I, except that the output inductor value is changed to 30 μH. First, the loss of a single GaN HEMT and a single inductor versus γ is depicted under different loads. After that, then related total losses versus γ can be obtained, which is then used to determine the optimal γ under different loads. Those results for both topologies are given in Figs. 23 and 24, respectively.

Considering the PU mode inverter, hybrid TCM will results in higher losses in high power level (>40%). Only at light loads, the hybrid control is better than TCM. This can be explained by the fact that, due to the low switching frequency, the decreased switching losses cannot compensate the increased conduction losses. As shown in Fig. 23(d), the highest switching frequency f_{swmax} is only several hundred kilohertz under heavy loads. However, when the output power decreases to 20% load, f_{swmax} approaches megahertz level and the related switching losses become significant, where the hybrid control can replace TCM for better performance.

For the SP mode inverter, the hybrid TCM control has a significant impact on the related losses, especially on GaN loss. As is shown in Fig. 24(c), the optimal γ under different loads, which are marked with different shaped symbols, increase as the output power decreases. Furthermore, the related highest switching frequency points also decrease from 3.3 MHz to about 1 MHz, which is presented in Fig. 24(d). After the inner optimization, the hybrid control always has lower losses and switching frequency than TCM.

C. Extension Optimization Results for Higher Power Density

On the basis of the above analysis, it can be concluded that hybrid TCM control is more suitable for the SP mode. Therefore, the discussion in this section is focused on the SP mode. This extension optimization algorithm is aimed to pick up the lowest output inductor value to achieve higher power density as much

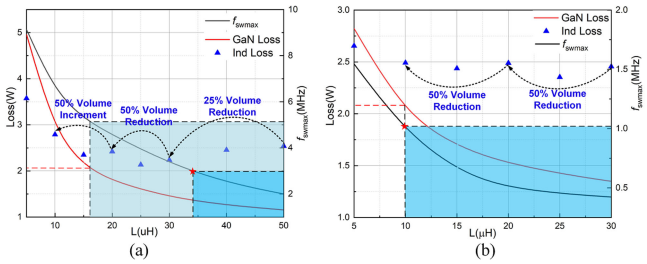

Fig. 25. (a) GaN losses, inductor losses and related highest switching frequency f_{swmax} versus the output inductor value L for TCM. (b) GaN losses, inductor losses and related highest switching frequency f_{swmax} versus the output inductor value L for hybrid TCM.

as possible. After the optimization algorithm is executed, the GaN HEMT loss, inductor loss, and related switching frequency for hybrid TCM are calculated and depicted in Fig. 25. Both GaN loss and switching frequency increase as the inductor value decreases. As for the inductor loss, it remains almost unchanged. This is because the inductor volume is reduced with lower inductor value. When the inductor value is lower than 10 μH, the related TCM switching frequency will become extremely high. The magnetic material for radio frequency is selected, which lead to a significant increment of the inductor volume and loss.

Therefore, the optimal output inductor value is mainly limited by two factors, including the switching frequency limit f_{lim} and the power dissipation limit P_{lim}. According to the literature [16], f_{lim} can be defined as 3.5 MHz. In this article, P_{lim} can be calculated as

$$P_{\mathrm{lim}} = \frac{T_J - T_{am}}{R_{\theta JA}} \tag{36}$$

where T_{J} is the limited junction temperature and T_{am} is the ambient temperature, while $R_{\theta \mathrm{JA}}$ is the junction-to-ambient thermal resistance. If both limits are determined, the optimal output inductor value can be obtained finally. The deeper-gray area represents the optional parameter range and the optimal point is marked by a pentagram. As is shown in Fig. 25(b), the deeper-gray area is limited by P_{lim} and the optimal output inductor value can be selected as 10 μH. In contrast, the deeper-gray area in TCM is limited by f_{lim} and the optimal inductor value is only 34 μH. In a conclusion, the optimal hybrid control can achieve higher power density than TCM.

VI. Experiment Results

A. Prototype of the Single-Phase Inverter

Finally, a single-phase inverter prototype is built with GaN HEMTs to verify the proposed hybrid TCM method, which is shown in Fig. 26. The design parameters of the converter are listed in Table II. The inverter topology is selected as the SP mode. For achieving high power density, the inverter is designed as a four-layer-stacked structure. It consists of the power board with semiconductors, the auxiliary supply and gate driver board, the measurement and control board, and the output stage board from bottom to top. To make the inverter more compact, the traditional large dc-link capacitor is replaced by an active power decoupling circuit [39]. The designed dc side decoupling circuit

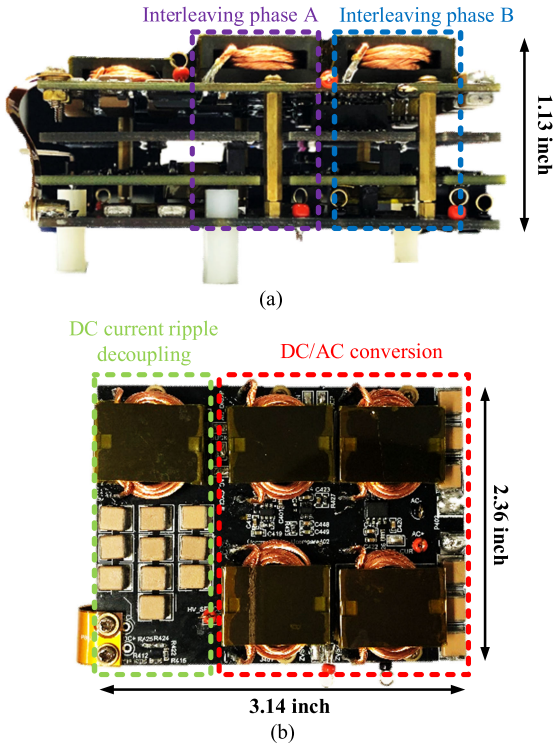

Fig. 26. Prototype of two-phase interleaved 1-kW megahertz single-phase inverter: (a) front view; (b) top view.

TABLE II
Parameters of the Prototype

Part.	Description	Value
Main Topology	Input voltage V_{dc}	400V
	Output voltage V_{orms}	220V,50Hz
	Rated output power P_o	1kW (4 leg)
	Switching frequency f_{sw}	300kHz-3MHz
	Output stage inductance L	34uH
	Filter capacitance C_f	3.3uF
Decoupling Circuit	Decoupling inductance L_d	30uH
	Buffer capacitance C_d	66uF
	Switching frequency f_d	300kHz
GaN HEMTs	Part No.	GS66502B
MCU	Part No.	TMS320F28379S
	Clock frequency F_{clk}	200MHz
	Control cycle T_{ISR}	5us

is configured by a synchronous buck converter with two GaN HMETs, a decoupling inductor, and buffer capacitors. The dc side current ripple can be compensated by storing/releasing the energy in/from the buffer capacitor. Compared with 0.5-mF bulk capacitors, the buffer capacitance is reduced to 66 μF. Furthermore, the two-phase interleaving technology is applied for higher power conversion. Finally, the rating power achieves 1 kW and the power density achieved by this prototype is around 120 W/in^3.

B. Verification of Inner Optimization Algorithm

Fig. 27 shows the typical experimental waveforms of both TCM and the hybrid TCM after inner optimization. From the switching-cycle waveforms at two instants, it can be known that

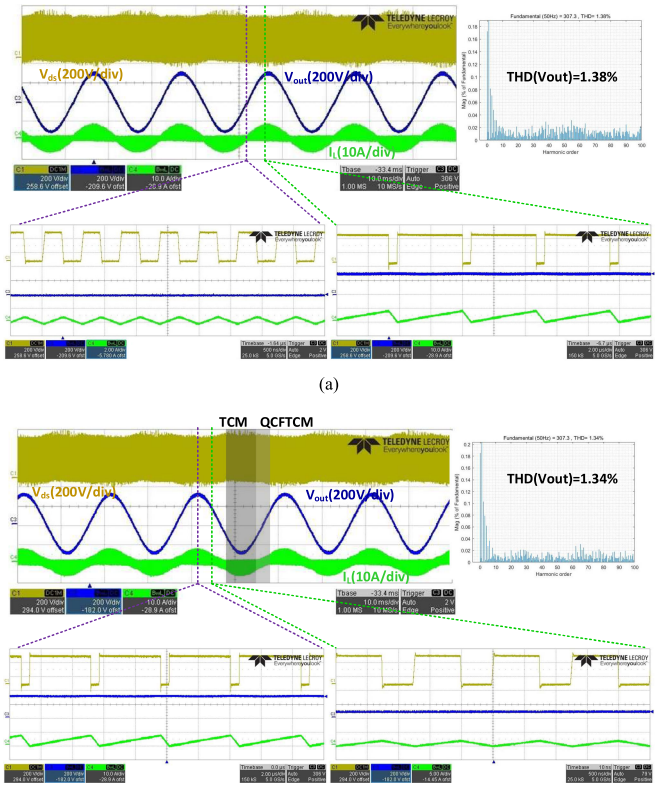

Fig. 27. (a) Experimental waveforms at 400 V_{dc}, 220 V_{ac}, when the inverter operates in pure TCM and related FFT analysis result of output voltage. (b) Experimental waveforms at 400 V_{dc}, 220 V_{ac}, when the inverter operates in optimal hybrid TCM and related FFT analysis result of output voltage.

ZVS is well maintained during the line cycle and the highest switching frequency is only about 1 MHz. When this inverter is controlled by pure TCM, the switching frequency will increase to 2.2 MHz, which is harder for digital-control implementation. The total harmonic distortion (THD) of the output voltage is also compared between TCM and hybrid TCM. Both are well controlled as sinusoidal shapes. Furthermore, THD of the output voltage is analyzed under different output power. As shown in Fig. 28, the THD in hybrid TCM is usually higher than that in TCM. However, when the inverter operates at light loads, the switching frequency of TCM over the line cycle will be close to the highest frequency. The digital control by DSP becomes not very accurate at this time, which leads to higher THD in TCM.

Large inductor current ripple is shown in the above waveforms and it will add to the burden and increase the size of output stage filter including EMI filter. Two-phase interleaving can also help to achieve better performance. Two phases usually operate with 180° phase shift to have the ripple cancellation benefit for the total output current. Fig. 29 shows the related waveforms of inductor currents and total current in phase A. It can be seen that good interleaving is achieved during the line cycle.

Fig. 30 is the measured total efficiency at 400 V_{dc} input and 220 V_{ac} output condition. The peak efficiency is close to 98% with the optimal hybrid TCM. Nearly the same efficiency is achieved in TCM. However, when the output power drops to

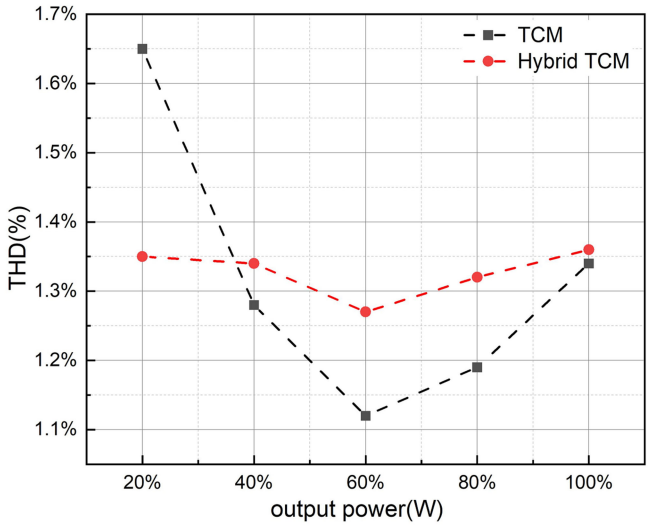

Fig. 28. Output voltage THD comparison between TCM and hybrid TCM.

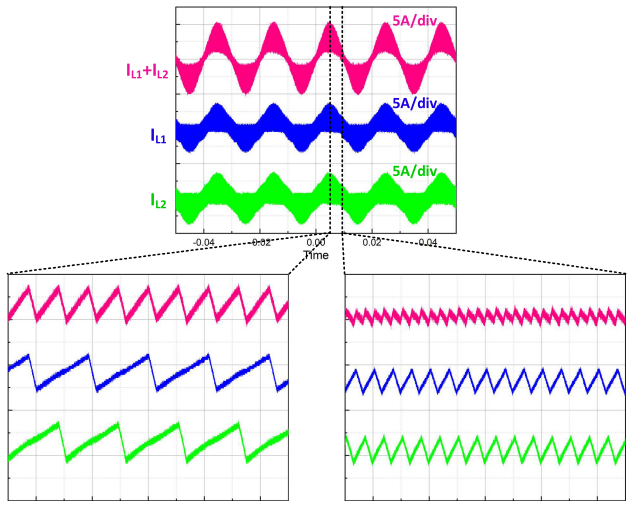

Fig. 29. Open-loop interleaving waveforms for eliminating the large current ripple.

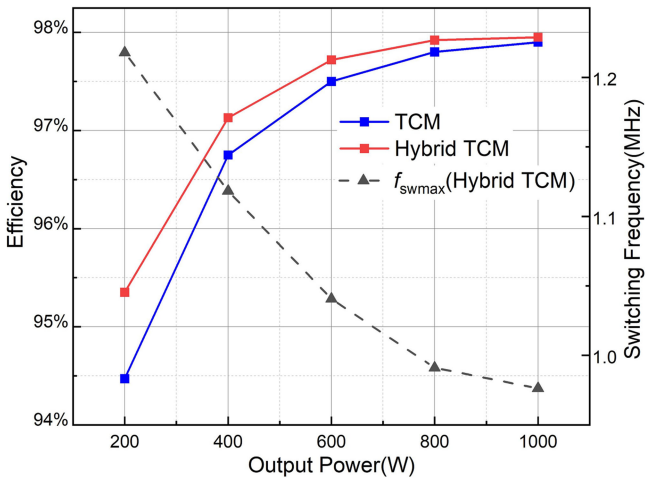

Fig. 30. Measured efficiency comparison between hybrid TCM and TCM.

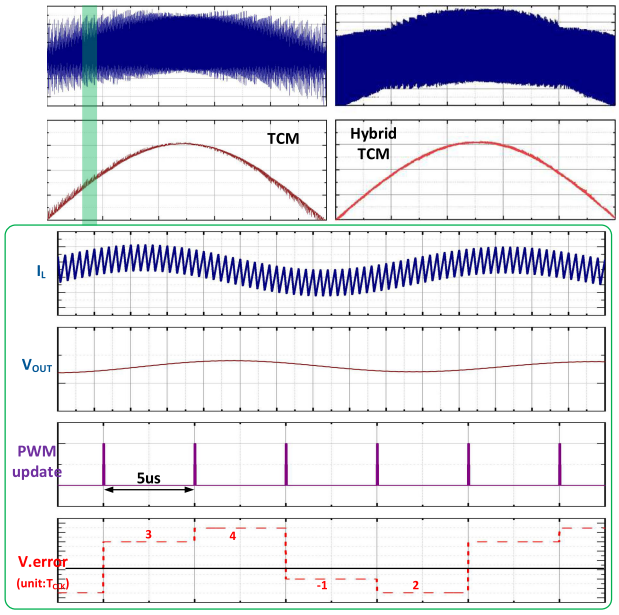

Fig. 31. Simulated closed-loop digital control of TCM and hybrid TCM when the inductance is 10 μH (V. error is the calculated voltage error between the reference voltage and the sampling voltage. The variable use digitalized and normalized value to the MCU clock cycles).

200 W, the measured efficiency of the hybrid TCM will become 0.8 % higher than TCM.

C. Verification of Extension Optimization Algorithm

According to Fig. 25, the output inductance can be reduced from 34 to 10 μH to improve the power density further in hybrid TCM. At this time, the switching frequency of TCM is up to 7 MHz, which is almost impossible to be implemented in both hardware and software. In terms of software level, both TCM and hybrid TCM control is implemented by a single MCU. Different control functions should be executed in a series, so that the total control cycle takes 1000 system clock cycle to complete. As shown in Table II, the total control cycle is 5 μs, which is longer than the switching cycle. Compared with hybrid TCM, the switching cycle in TCM is much smaller than the control cycle. When the same control interrupt is executed, a severe voltage error oscillation will occur. Fig. 31 shows the simulation waveform. There is a significant oscillation in TCM inductor current, which lead to very high THD of the output voltage. In contrast, the inductor current in hybrid TCM is controlled very well due to much lower switching frequency.

As for hardware level, the suitable core material is also a challenge for TCM. At such a high frequency, most magnetic core used for power conversion will cause very high losses. If the TCM inductor is designed by core material for radio frequency, the size of the inductor will increase due to much lower permeability. In contrast, the inductor for hybrid TCM can be designed more impact due to the lower switching frequency. The new designed inductor for hybrid TCM has 50% volume reduction, which is shown in Fig. 32. The power density with unchanged boards increases to 135 W/in^3. If the related PCB board is redesigned for new inductors, the power density is

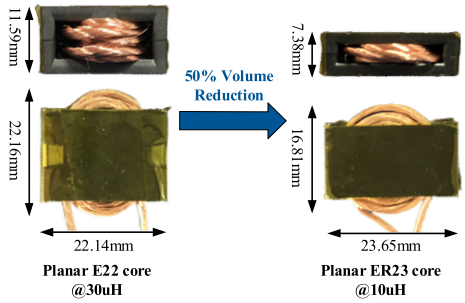

Fig. 32. Output inductor volume reduction for higher power density in hybrid TCM.

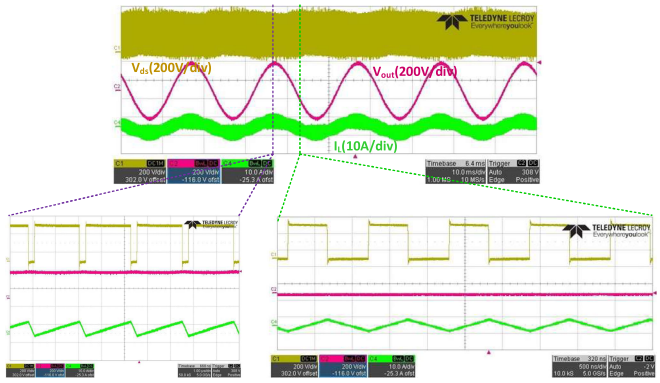

Fig. 33. Experimental waveforms at 400 $V_{\rm dc}$, 220 $V_{\rm acrms}$, when the inverter operates in optimal hybrid TCM for higher power density.

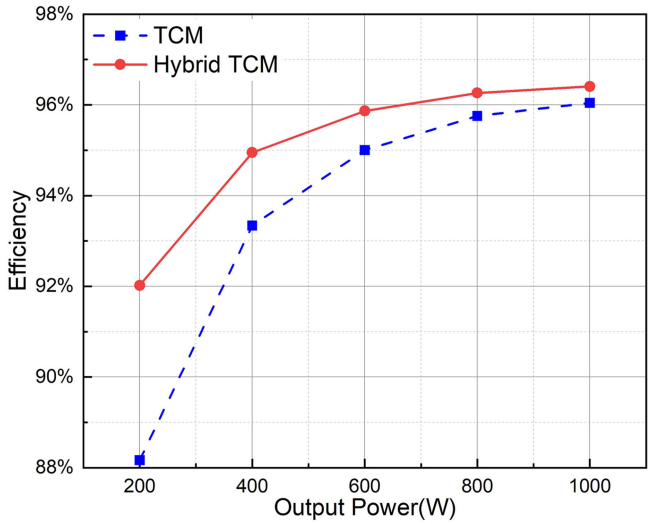

Fig. 34. Comparison between measured efficiency for hybrid TCM and calculated efficiency for TCM.

estimated to be 192 W/in^3 through 3-D CAD simulation. In this article, all the experimental results are based on the same PCB boards.

Fig. 33 shows the typical experimental waveforms of the hybrid TCM after extension optimization. More QCFTCM region is operated and the highest switching frequency is managed to 1.2 MHz. Fig. 34 shows the related measured efficiency at 400 Vdc input and 220 Vac output condition. Due to the extremely high switching frequency of TCM (up to 10 MHz) at this time,

the calculated TCM efficiency is given for comparison. It can be seen that the efficiency of hybrid TCM is always higher than TCM. Especially under light load conditions, the efficiency of hybrid TCM is nearly 4% higher than TCM.

VII. Conclusion

It can be concluded that the huge variation of switching frequency in a TCM-based symmetrical inverter will yield excessive switching losses and decrease the overall efficiency, especially under light load conditions. Through the hybrid TCM control with ZVS turn ON proposed in this article, the extremely high switching frequency range can be eliminated and the efficiency can remain almost the same as the pure TCM operation at rated power, even higher under light loads. On the other hand, the hybrid TCM will expand the limits of related parameter design and further increase the power density. Finally, an interleaved megahertz single-phase inverter is implemented to verify the proposed method. The power density achieves 120 W/in^3, and the peak efficiency is up to 98%.

Appendix

Before calculating the related core loss, the parameters of the designed inductor are given below.

Winding turns N; Core path length L_e; Core permeability μ.

For the LF component, the peak flux density is calculated as

$$B_{pk} = \mu \frac{N\sqrt{2} I_{\text{load}}}{L_e}. \tag{A1}$$

Substitute (A1) into (29), the LF core losses for Both TCM and Hybrid TCM are given as

$$P_{c,HF} = V_c k f_{\text{line}}^{\alpha} \cdot (\mu \frac{N\sqrt{2} I_{\text{load}}}{L_e})^{\beta}. \tag{A2}$$

As for the HF component, the related the ac flux swing ΔB for TCM and QCFTCM section can be calculated respectively,

$$\Delta B_{(t)} = \mu \frac{N\sqrt{2} I_{\text{load}} \sin \omega t}{L_e} \tag{A3}$$

$$\Delta B_{(q)} = \mu \frac{N(I_{\text{peak}(q)}(t) + I_{neg(q)}(t))}{2L_e}. \tag{A4}$$

Substitute (A3) and (A4) into (30), the HF core losses for Hybrid TCM are given as

$$\begin{aligned} P_{c,HF} = Q \cdot & \int_{\frac{\gamma T_{\text{line}}}{4}}^{\frac{T_{\text{line}}}{2} - \frac{\gamma T_{\text{line}}}{4}} f_{sw(t)}(t)^{\alpha} \cdot (\sqrt{2} I_{\text{load}} \sin \omega t)^{\beta - \alpha} dt \\ & + 2Q \cdot \int_{0}^{\frac{\gamma T_{\text{line}}}{4}} f_{sw(q)} \left(\frac{\gamma T_{\text{line}}}{4} \right)^{\alpha} \\ & \cdot \left(\frac{I_{\text{peak}(q)}(t) + I_{neg(q)}(t)}{2} \right)^{\beta - \alpha} dt \end{aligned} \tag{A5}$$

with $Q = \frac{2V_c k_i}{T_{\text{line}}} \cdot (\frac{\mu N}{L_e})^{\beta - \alpha}$. When γ is equal to zero, the conduction loss for TCM control can also be obtained.

References

[1] Q. Li and P. Wolfs, "A review of the single-phase photovoltaic module integrated converter topologies with three different dc link configurations," *IEEE Trans. Power Electron.*, vol. 23, no. 3, pp. 1320–1333, May 2008.

[2] Y. Xue, L. Chang, S. B. Kjaer, J. Bordonau, and T. Shimizu, "Topologies of single-phase inverters for small distributed power generators: An overview," *IEEE Trans. Power Electron.*, vol. 19, no. 5, pp. 1305–1314, Sep. 2004.

[3] Z. J. Zhou, X. Zhang, P. Xu, and W. X. Shen, "Single-phase uninterruptible power supply based on Z-source inverter," *IEEE Trans. Ind. Electron.*, vol. 55, no. 8, pp. 2997–3004, Aug. 2008.

[4] Solar inverters, ABB, 2020. [Online]. Available: http://new.abb.com/power-converters-inverters/ solar

[5] Solar inverters, SMA, 2020. [Online]. Available: https://www.sma.de/en/products/solarinverters. html

[6] PV inverters, Sungrow, 2020. [Online]. Available: https://en.sungrowpower.com/index.php/en/ products/residential

[7] Single phase string inverters, Solax Power, 2020. [Online]. Available: https://krannich-solar.com/ fileadmin/content/pdf/International/Solax_X_Phasen_Wechselrichter_eng.pdf

[8] U. K. Mishra, P. Parikh, and Y. Wu, "AlGaN/GaN HEMTs—An overview of device operation and applications," *Proc. IEEE*, vol. 90, no. 6, pp. 1022–1031, Jun. 2002.

[9] N. Ikeda, S. Kaya, J. Li, Y. Sato, S. Kato, and S. Yoshida, "High power AlGaN/GaN HFET with a high breakdown voltage of over 1.8 kV on 4-inch Si substrates and the suppression of current collapse," in *Proc. 20th Int. Symp. Power Semicond. Devices*, 2008, pp. 287–290.

[10] J. Millan, P. Godignon, X. Perpina, A. Perez-Tomas, and J. Rebollo, "A survey of wide bandgap power semiconductor devices," *IEEE Trans. Power Electron.*, vol. 29, no. 5, pp. 2155–2163, May 2014.

[11] E. Persson, "How 600 V GaN transistors improve power supply efficiency and density," *Power Electron. Eur.*, vol. 2, pp. 21–24, Mar. 2015.

[12] E. Gurpinar and A. Castellazzi, "Single-phase T-type inverter performance benchmark using si IGBTs, SiC MOSFETs, and GaN HEMTs," *IEEE Trans. Power Electron.*, vol. 31, no. 10, pp. 7148–7160, Dec. 2015.

[13] C. Lin, Y. Liu, J. Lai, and B. Chen, "High-voltage GaN HEMT evaluation in micro-inverter applications," in *Proc. IEEE Appl. Power Electron. Conf. Expo.*, 2015, pp. 2474–2480.

[14] H. Li *et al.*, "Design of a 10 kW Gan-based high power density three-phase inverter," in *Proc. IEEE Energy Convers. Congr. Expo.*, 2016, pp. 1–8.

[15] C. Marxgut, J. Biela, and J. W. Kolar, "Interleaved triangular current mode (TCM) resonant transition, single phase PFC rectifier with high efficiency and high power density," in *Proc. Int. Power Electron. Conf.*, 2010, pp. 1725–1732.

[16] Z. Liu, F. C. Lee, Q. Li, and Y. Yang, "Design of GaN-based MHz totem-pole PFC rectifier," *IEEE J. Emerg. Sel. Top. Power Electron*, vol. 4, no. 3, pp. 799–807, May 2016.

[17] Z. Liu, B. Li, F. C. Lee, and Q. Li, "Design of CRM AC/DC converter for very high-frequency high-density WBG-based 6.6kW bidirectional on-board battery charger," in *Proc. IEEE Energy Convers. Congr. Expo.*, 2016, pp. 1–8.

[18] L. Huber, B. T. Irving, and M. M. Jovanovic, "Effect of valley switching and switching-frequency limitation on line-current distortions of DCM/CCM boundary boost PFC converters," *IEEE Trans. Power Electron.*, vol. 24, no. 2, pp. 339–347, Dec. 2009.

[19] N. Haryani, R. Burgos, and D. Boroyevich, "Variable frequency and constant frequency modulation techniques for GaN based MHz H-bridge PFC," in *Proc. IEEE Appl. Power Electron. Conf. Expo.*, 2015, pp. 1889–1896.

[20] A. C. Schittler, D. Pappis, and P. Zacharias, "EMI filter design for high switching speed and frequency grid-connected inverters," in *Proc. ECCE Eur.*, 2016, pp. 1–8.

[21] X. Gong, I. Josifović, and J. A. Ferreira, "Modeling and reduction of conducted EMI of inverters with SiC JFETs on insulated metal substrate," *IEEE Trans. Power Electron.*, vol. 28, no. 7, pp. 3138–3146, Oct. 2012.

[22] M. Yang *et al.*, "Resonance suppression and EMI reduction of GaN-based motor drive with sine wave filter," *IEEE Trans. Ind. Electron.*, vol. 56, no. 3, pp. 2741–2751, Jun. 2020.

[23] A. Majid, J. Saleem, F. Alam, and K. Bertilsson, "Analysis of radiated EMI for power converters switching in MHz frequency range," in *Proc. IEEE Int. Symp. Diagnostics Elect. Mach., Power Electron. Drives*, 2013, pp. 428–432.

[24] "Mn-Zn Ferrite Power Core, " DMEGC, Hengdian, China, 2020. [Online]. Available: http://www.chinadmegc.com/en/products_list.php?2

[25] "Mn-Zn Ferrite Material characteristics, " TDK, Tokyo, Japan, 2020. [Online]. Available: https://product.tdk.com/info/en/catalog/datasheets/ferrite_mn-zn_material_characteristics_en.pdf
[26] "Mn-Zn Ferrite for Power Conversion," Ferroxcube, Hamburg, Germany, 2020. [Online]. Available: https://www.ferroxcube.com/en-global/ak_material/index/power_conversion#6
[27] M. Hartmann, S. D. Round, H. Ertl, and J. W. Kolar, "Digital current controller for a 1 MHz, 10 kW three-phase VIENNA rectifier," *IEEE Trans. Power Electron.*, vol. 24, no. 11, pp. 2496–2508, 2009.
[28] M. Fernandez-Gomez, C. Fernandez, P. Zumel, A. Sanchez, and A. d. Castro, "Design of DPWM with high resolution under 80 ps using low-cost xilinx FPGA," *Proc. IEEE Appl. Power Electron. Conf. Expo.*, 2020, pp. 3043–3048.
[29] Z. Yi, Y. Tan, T. Liu, C. Chen, and Y. Kang, "Experimental study on gate drive influence to the 650 V GaN E-HEMT," in *Proc. PCIM Eur.*, 2018, pp. 963–968.
[30] R. Chen and S. Yu, "A high-efficiency high-power-density 1MHz LLC converter with GaN devices and integrated transformer," in *Proc. IEEE Appl. Power Electron. Conf. Expo.*, 2018, pp. 791–796.
[31] A. Nawawi *et al.*, "Design of high power density converter for aircraft applications," in *Proc. Int. Conf. Elect. Syst. Aircr., Railway, Ship Propulsion Road Veh.*, 2015, pp. 1–6.
[32] Z. Huang, Z. Liu, Q. Li, and F. C. Lee, "Microcontroller-based MHz totem-pole PFC with critical mode control," in *Proc. Energy Convers. Congr. Expo.*, 2016, pp. 1–8.
[33] J. Wang, H. S. h. Chung, and R. T. h. Li, "Characterization and experimental assessment of the effects of parasitic elements on the MOSFET switching performance," *IEEE Trans. Power Electron.*, vol. 28, no. 1, pp. 573–590, Apr. 2013.
[34] P. Nayak and K. Hatua, "Modeling of switching behavior of 1200 v SiC MOSFET in presence of layout parasitic inductance," in *Proc. IEEE Int. Conf. Power Electron., Drives Energy Syst.*, 2016, pp. 1–6.
[35] M. R. Ahmed, R. Todd, and A. J. Forsyth, "Predicting SiC MOSFET behavior under hard-switching, soft-switching, and false turn-on conditions," *IEEE Trans. Ind. Electron.*, vol. 64, no. 11, pp. 9001–9011, Aug. 2017.
[36] J. Muhlethaler, J. Biela, J. W. Kolar, and A. Ecklebe, "Core losses under the DC bias condition based on Steinmetz parameters," *IEEE Trans. Power Electron.*, vol. 27, no. 2, pp. 953–963, Jun. 2012.
[37] J. Muhlethaler, "Modeling and multi-objective optimization of inductive power components," ETH Zurich, Switzerland, Ph.D. dissertation, 2012.
[38] R. M. Burkart, H. Uemura, and J. W. Kolar, "Optimal inductor design for 3-phase voltage-source PWM converters considering different magnetic materials and a wide switching frequency range," in *Proc. Int. Power Electron. Conf.*, 2014, pp. 891–898.
[39] R. Wang *et al.*, "A high power density single-phase PWM rectifier with active ripple energy storage," *IEEE Trans. Power Electron.*, vol. 26, no. 5, pp. 1430–1443, May 2011.

Teng Liu (Student Member, IEEE) received the B.S. degree in electrical engineering and automation in 2016 from the School of Electrical and Electronic Engineering, Huazhong University of Science and Technology, Wuhan, China, where he is currently working toward the Ph.D. degree.

His current research interests include high frequency power conversion techniques and applications of wide bandgap power semiconductor devices.

Cai Chen (Member, IEEE) received the B.S. and Ph.D. degrees in electrical and electronic engineering from Huazhong University of Science and Technology, Wuhan, China, in 2008 and 2014, respectively.

He is an Associate Research Fellow with the Huazhong University of Science and Technology. From March to December 2013, he was an Intern in GE Global Research Center, Shanghai, China. From 2014 to 2016, he joined the Advanced Semiconductor, Packaging and Integration Lab, Huazhong University of Science and Technology, Wuhan, Hubei, China, as a Postdoctoral Researcher. From 2016 to 2017, he was a Visiting Scholar with the Center for High Performance Power Electronics, The Ohio State University, Columbus, OH, USA. From 2017 to 2018, he was a Visiting Scholar with the College of Engineering, University of Arkansas, Fayetteville, AR, USA. In 2019, he joined the Huazhong University of Science and Technology, Wuhan, China, as an Associate Research Fellow. His research interests include WBG devices packaging, integration, packaging EMI issues, packaging reliability and high-density applications.

Ke Xu received the B.S. degree in electrical engineering from the Huazhong University of Science and Technology, Wuhan, China, where he is currently working toward the M.S. degree with the School of Electrical and Electronic Engineering.

His research interests include high-frequency power conversion techniques, digital control and modeling of converters.

Yi Zhang received the B.S. degree in electrical and electronic engineering in 2016 from Huazhong University of Science and Technology, Wuhan, China, where he is currently working toward the Ph.D. degree with the School of Electrical and Electronic Engineering.

His current research interests include wide bandgap power devices, high-density applications, and switching behavior modeling.

Yong Kang (Senior Member, IEEE) received the B.E., M.E, and Ph.D. degrees from the Huazhong University of Science and Technology, Wuhan, China, in 1988, 1991, and 1994, respectively.

In 1994, he joined the Huazhong University of Science and Technology, as a Lecturer and was promoted to Associate Professor in 1996 and Full Professor in 1998. He is the author of more than 60 technical papers. His research interests include power electronic converter, ac drivers, electromagnetic compatibility, their digital control techniques, WBG device packaging and applications.